

1
2
3
4
5
6
7
8
9
10
11
12
13
14
15
16
17
18
19
20
21
22
23
24

Revision 2

**MINERALOGY AND CHEMISTRY OF SAN CARLOS HIGH-ALKALI
BASALTS: ANALYSES OF ALTERATION WITH APPLICATION FOR MARS
EXPLORATION**

Bryné A. Hadnott^{1,2*}, Bethany L. Ehlmann^{2,3}, Bradley L. Jolliff¹

1. Department of Earth and Planetary Sciences, Washington University in St. Louis, St.
Louis, MO

2. Division of Geological and Planetary Sciences, California Institute of Technology,
Pasadena, CA

3. Jet Propulsion Laboratory, California Institute of Technology, Pasadena, CA

* now at Department of Earth and Atmospheric Sciences Cornell University, Ithaca, NY.

Correspondence to: Rm 414 Spaces Sciences Building, Cornell University 122 Garden
Avenue, Ithaca, NY 14853, bah248@cornell.edu

Keywords: VSWIR spectroscopy, Mars analogs, XRD, geochemistry, alkali basalts, San
Carlos

25

26 **Abstract**

27 The discovery of Fe, Mg, and Al phyllosilicate clays on Mars using visible and shortwave
28 infrared (VSWIR) spectroscopy from orbit indicates aqueous alteration of basaltic rocks.
29 Analyses at Gusev Crater by the Spirit rover and Gale Crater by the Curiosity rover have
30 discovered alkaline basaltic rocks. In this work, multiple methods—VSWIR spectroscopy,
31 x-ray diffraction (XRD), and chemical analyses—were used to study a suite of alkaline
32 basalts from San Carlos, AZ, which have been altered by water in an oxidative, semi-arid
33 environment. As an analog for the weathering of alkaline basaltic rocks on Mars, a suite
34 of rocks visually identified to have different degrees of alteration were characterized to
35 understand the spectral, mineralogical and chemical trends in alteration as sensed by
36 multiple techniques. Samples with strong 1.9- μm H₂O-related absorptions in VSWIR
37 commonly exhibited absorption bands at 1.4, 2.2, and/or 2.3 μm , indicating the presence
38 of clay minerals or silica as well as features at 0.5-0.9 μm indicative of ferric iron oxides.
39 Primary mineralogy for all samples, as determined by point analyses with the microprobe
40 and XRD, consisted of olivine, plagioclase, nepheline, augite, and titanomagnetite.
41 Compositional imaging and spot analyses with the microprobe revealed distinct alteration
42 textures and phases, suggesting weathering pathways involving the oxidation of iron in
43 olivine and primary Fe(II) oxides to form Fe(III) oxides as well as the formation of
44 aluminum phyllosilicates and magnesium phyllosilicates from feldspars and olivines,
45 respectively, while pyroxene remained relatively unaltered. Bivariate plots of major
46 oxides both from bulk chemical analysis and microprobe measurements also revealed
47 trends in alkali and silica depletion and calcium enrichment, but there was little chemical

48 fractionation in most of the major oxides. The strength of the 1.9- μm H₂O absorption,
49 loss on ignition, and depletion in silica and sodium, correlated with increasing alteration.
50 The datasets provide an analog for understanding possible weathering pathways in
51 martian alkaline basalts and thresholds for the detection of aqueous alteration in multiple
52 datasets.

53

54 **1.0 Introduction**

55 Orbiting visible and near-infrared spectrometers, and data from landed missions, have
56 revealed a diverse array of aqueous environments preserved in the rock record from
57 ancient Mars. The vast majority of the surface of Mars is basaltic in composition [e.g.,
58 *Rogers and Christensen et al., 2007*] but sulfates, chlorides, carbonates, and hydrated
59 silicates have been detected by orbiting spectrometers and confirmed by rover data [e.g.,
60 *Bibring et al., 2006; Mustard et al., 2008; Ehlmann & Edwards, 2014; Grotzinger et*
61 *al., 2015*]. Currently, the Mars Science Laboratory Curiosity rover is exploring Gale
62 Crater, a site that hosts a diverse array of lithologies, including suites of rocks that are
63 more alkali-rich than other martian basalts, as revealed by analyses with the ChemCam
64 Laser-Induced Breakdown Spectroscopy instrument (LIBS) [*Wiens et al., 2012, 2013;*
65 *Maurice et al., 2012; Cousin et al., 2015; Sautter et al., 2015; Vasavada et al., 2014*] and
66 the Alpha Particle X-ray Spectrometer (APXS) [*Gellert et al., 2013*]. Jake Matijevic, the
67 first target analyzed by both ChemCam and APXS, is interpreted to be a fine-grained
68 igneous rock with an alkaline composition similar to nepheline-normative mugearites
69 [*Stolper et al., 2013; Blaney et al., 2014*]. Three other rock targets, and multiple other
70 rocks and clasts measured remotely by ChemCam, were found to have alkaline basalt

71 compositions and to plot in the basanite field on a total alkali silica (TAS) diagram
72 (Figure 1), suggesting alkali-rich igneous protoliths as source material for sedimentary
73 rocks and a greater diversity of martian igneous compositions [*Schmidt et al.*, 2014;
74 *Meslin et al.*, 2013; *Sautter et al.*, 2014]. Similarly, alkaline suites of rocks have also been
75 measured in the Columbia Hills, Gusev crater by the Spirit rover [*McSween et al.*, 2006].
76 Collectively, these data suggest unique types of martian volcanism and/or aqueous
77 alteration to explain their geochemistry [*McSween et al.*, 2006; *Schmidt et al.*, 2014; *Udry*
78 *et al.*, 2014].

79

80 To date, most spectral libraries and analyses of aqueous alteration of igneous protoliths as
81 Mars analogs have focused on subalkaline basalts [e.g., *Golden et al.*, 2005; *Hurowitz et*
82 *al.*, 2005; 2007; *Hausrath et al.*, 2008; *Ehlmann et al.*, 2012; *Greenberger et al.*, 2012].
83 Few analog studies of alkaline basalts exist, but these have become relevant to the
84 interpretation of returned data, given the finding of Spirit and Curiosity rovers, as
85 described above. Thus, there are two goals of this work: (1) the study of aqueous
86 alteration of specifically alkaline basalts as Mars analogs and (2) the collection of laser-
87 induced breakdown spectroscopy (LIBS) data of well-characterized and Mars-relevant
88 samples to improve the ability of ChemCam to quantify elemental composition and
89 identify signs of aqueous alteration in minerals and soils at Gale Crater. For the latter
90 objective, ChemCam uses a partial least squares (PLS) approach to determine the
91 geochemistry of martian rock samples based on a library of known standards [*Clegg et al.*,
92 2009; *Wiens et al.*, 2013]. PLS works best when the library samples closely match the
93 composition of materials being observed [*Clegg et al.*, 2009; 2014; in review]. Hence, the

94 rocks described and characterized here were used to supplement others to create a
95 new, >400 sample database [Clegg et al., 2014; in review] from the previous library size
96 of 72 [Wiens et al., 2013]. Here we report on (1).

97

98 We used multiple laboratory techniques to characterize a suite of 2 -3 Myr basalt flows
99 from San Carlos, AZ. Waters had interacted with the samples, causing oxidative
100 weathering and some clay formation. Samples collected from the flows exhibited a range
101 in alteration extent and/or style, indicated to first order by varying amounts of reddish-
102 brown material on the rock surface, extending into the interior. The San Carlos suite was
103 chosen as an analog for alteration of alkaline basalts on Mars due to the similarities in
104 original rock lithology and the fact that alteration appeared to be minor. The semi-arid
105 environment is likely warmer than that at the Mars surface, thus speeding reaction
106 kinetics, but the relatively small degree of alteration offered the chance to study in detail
107 the early stages of chemical breakdown of an alkaline basalt. Visible and shortwave
108 infrared (VSWIR) spectra, X-ray diffraction (XRD), bulk chemistry, and electron
109 microprobe data were collected from this suite of basalts. The data was used to identify
110 all primary minerals and their compositions, estimate bulk composition and mineralogy,
111 characterize alteration by identifying various minerals and alteration reactions, and
112 provide information on past weathering processes, as well as primary compositions.
113 Following sample characterization, the San Carlos basalt suite was measured by LIBS, in
114 both whole rock and compressed pellet forms, for addition to the ChemCam library
115 [Ehlmann et al., 2013; Clegg et al., 2014; in review]. Here, using the suite of techniques,

116 we determine the primary and secondary mineralogy and chemical alteration pathways of
117 the San Carlos rocks.

118

119 **2.0 Geologic Setting and Samples**

120 Six of the seven samples were collected from the San Carlos ultramafic inclusion locality,
121 in Peridot Canyon, San Carlos, Arizona (Figure 2). Peridot Mesa, incised by the canyon,
122 is composed of late Tertiary or early Quaternary basalt flows. One sample was
123 purchased from the same locality in order to obtain a pristine, least weathered rock and
124 may be from a slightly different locale than the rest of the suite. Bright green ultramafic
125 xenoliths, largely olivine, are widespread throughout the locality, occurring as large
126 gravity-settled masses in the basaltic flows. The host rock is fine-grained and consists of
127 plagioclase laths with smaller grains of pyroxene, nepheline, leucite, and titanomagnetite;
128 small olivine xenocrysts are also present [*Frey and Prinz, 1978*]. All samples exhibit
129 various degrees of weathering as evidenced by differences in color and reaction
130 boundaries between the host rock and xenolith. Highly altered basalts appear rust-colored,
131 whereas less altered basalts appear gray. The rust colored texture on the exterior of the
132 rock was analyzed in thin sections and identified as a rind, which we define as an
133 alteration horizon with a gradation from altered to more pristine material. In contrast,
134 coatings are deposited from external sources, and are discontinuous with the surface of
135 the rock [*Salvatore et al., 2013*]. Only sample F has an identifiable coating of gypsum.
136 The size of each sample varies from about a quarter of a meter to fist-sized (Figure 2).
137 For this work, we focus on the basaltic host rock, rather than the olivine-rich xenoliths.

138

139 **3.0 Methods**

140 **3.1 VSWIR Spectral Measurements**

141 The suite of basalts was labeled and photo-documented under normal lab conditions.
142 Also, written descriptions of each rock were made prior to further analysis. The suite of
143 sample rocks was then measured under ambient lab conditions using an Analytical
144 Spectral Devices (ASD) spectrometer with a contact probe attachment to obtain visible
145 and shortwave-infrared reflectance spectra from 0.4 to 2.5 μm . Spectra were calibrated to
146 reflectance using a Spectralon™ reflectance standard. Data were acquired from multiple
147 surfaces on each rock in order to assess sample heterogeneity.

148

149 The spectral continuum, i.e., overall shape, is an indicator of the style and degree of
150 alteration. Changes in overall continuum shape from flat to downward-sloping to curved
151 and concave down are related to the style and intensity of rock alteration. Negative slopes
152 between 0.75 and 1.0 μm indicate NIR “blue” slopes (decreasing reflectance with
153 increasing wavelength); positive slopes between the same range indicate NIR “red”
154 slopes (increasing reflectance with increasing wavelength) [e.g., *Farrand et al., 2006*]. In
155 terms of styles of alteration, an overall concave down slope over the 0.4-2.5 μm range,
156 i.e., initially increasing reflectance then decreasing reflectance with increasing
157 wavelength, suggests the presence of Fe(III) oxides and strong UV/visible absorptions to
158 create the initial upward continuum slope to $\sim 1.5\text{-}2.0$ μm and hydrated silicates with
159 strong 3 μm H₂O- and OH-related absorptions that create the downward sloping
160 continuum to longer wavelengths. In contrast, an overall negative slope (for basaltic
161 materials) suggests a coating or powder obscuring the surface, possibly a thin coating of

162 silica [e.g., *Mustard et al., 2005; Minitti et al., 2007; Skok et al., 2010*], and the underlying
163 rock need not be significantly altered.

164 The spectra were also examined for absorptions due to primary and secondary minerals.
165 Broader features nearer 1.0 μm and from 1.8- 2.2 μm are due to electronic transitions of
166 Fe(II) in pyroxenes. Features centered at 1.0 μm and 2.2 μm indicate high-Ca pyroxenes,
167 whereas broad absorptions at 0.90 μm and 1.90 μm indicate low-Ca pyroxenes [*Sunshine*
168 *& Pieters, 1993*]. Iron oxides have absorptions in the UV region and near 0.9 μm . Steep
169 positive slopes at wavelengths less than 0.50 μm and from 0.6 to 0.8 μm indicate the
170 presence of ferric iron oxides, which are weathering products; long wavelength features
171 near 0.9 μm also indicate well-crystalline ferric iron oxides. Hematite is distinguished by
172 an electronic transition at 0.86 μm . Goethite has a similar feature between 0.9 and 0.93
173 μm [*Morris et al., 2000*]. Phyllosilicates and clay mineralogy are indicated by a
174 combination of OH stretching and metal-OH bending between 2 and 2.5 μm . Absorptions
175 near 2.2 μm indicate Si-OH or Al-OH in phyllosilicates and opaline silica. For Al-rich
176 clays such as montmorillonite, the Al-OH absorption occurs at 2.21 μm and is sharper
177 than the Si-OH absorption in silica. Fe-OH is indicated by absorptions near 2.29 μm , and
178 absorptions around 2.31 μm indicate Mg-OH. An absorption near 1.9 μm indicates an H-
179 O-H bend and OH stretch caused by the presence of molecular H₂O in clay interlayers
180 [*Bishop et al., 1994*]. Bands near 1.4 μm indicate the first overtone of the OH stretch and
181 H₂O combinations [*Bishop et al., 2008; Clark et al., 1990; Clark et al., 2007a*].

182

183 Band depth calculations for the 0.53, 1.9, 2.2, and 2.3 micron absorptions in host basalt
184 spectra were determined using ENVI. Spectra were continuum-removed, and the

185 absorption of each identified band was measured by manually finding the band center in
186 the continuum-removed spectra. In this work, we used the CRISM defined band
187 parameters BD530, BD1900, BD2210, and BD2290 to measure continuum-removed
188 band strengths [Pelkey et al., 2007]. Quantification of these band depths provides
189 information on relative water content, ferric iron content, and metal-hydroxide content
190 (Table 2).

191

192 ***3.2 Preparation for Geochemical Analyses***

193 After spectral measurements were taken, a subset of samples was chosen based on
194 diversity in types of aqueous alteration, weathering products, and degree of alteration, as
195 evident from both the spectral properties and visual analysis. A small portion of each
196 sample within the subset was selected for preparation of polished thin sections,
197 impregnated with epoxy, and allowed to cure overnight. The purpose of the epoxy
198 impregnation was to preserve any coatings or alteration rinds present on the rock, which
199 affect VSWIR spectral properties and would otherwise have been washed away or
200 abraded during thin section preparation. Locations of thin-section cuts were selected to
201 include a wide variety of minerals, each representing the different spectral classes of
202 materials. Ideal portions contained surfaces and interior portions of both host rock and
203 xenoliths, though only the host rock is the focus of this study. The intent of the thin-
204 section analysis was to determine the chemical composition of mineral phases present
205 and to examine textural relationships between primary and secondary minerals.

206

207 The San Carlos host rocks were also analyzed for bulk chemical composition (major,
208 minor, and trace elements). Rocks were somewhat heterogeneous from visual indicators
209 of aqueous alteration, so representative parts of the host rock of each sample that did not
210 have an alteration rind and that lacked xenoliths were chipped off using a rock hammer
211 and chisel or rock saw. The intent of the bulk rock measurement was to compare the
212 chemistry across rock samples and to test for trends corresponding to degree of alteration,
213 measuring the composition and degree of alteration of the basalts only, not xenoliths, and
214 leaving analysis of any potential rinds for microprobe work.

215

216 ***3.3 Bulk Chemical Analysis***

217 Bulk chemical analysis was performed by Activation Labs, Ltd. in Ontario, Canada. Bulk
218 rock chips were powdered and mixed with Li metaborate and Li tetraborate flux in
219 graphite crucibles. The mixture was fused in a furnace at 1150° C and the resulting fused
220 material was dissolved in a mixture with 5 % nitric acid. Fused samples were then diluted
221 and analyzed with Perkin Elmer Sciex ELAN 6000, 6100 or 9000 ICP/MS. For every
222 group of samples, three blanks, three controls before the sample group, and two blanks
223 after the sample group were run. Duplicates were analyzed after every 15 samples and the
224 instrument was calibrated every 40 samples. Total Fe is reported as Fe₂O_{3T} for these data
225 because of oxidation during the fusion process.

226

227 ***3.4 Electron Microprobe***

228 The thin sections were first observed using a petrographic microscope to survey rock
229 textures and alteration and to identify areas of interest. The host rock (basanite) is

230 composed mainly of fine-grained pyroxene, plagioclase, and olivine. Xenoliths are
231 almost entirely composed of coarse-grained olivine with some pyroxene and opaque
232 minerals. Samples were then placed in a vacuum carbon evaporator and coated with a
233 thin layer of conductive carbon. Electron microprobe measurements were done with the
234 JEOL JXA-8200 at Washington University in St. Louis. Measurements were made using
235 a 15 KV accelerating potential, 25 nA beam current, and a range of beam sizes from 1 to
236 10 micrometers, depending on the grain size and the susceptibility of a grain to
237 volatilization. Both reflected light and back-scattered electron imaging were used to
238 search for textures caused by alteration and to focus the beam for analyses of elemental
239 abundances. Energy-dispersive spectrometry (EDS) was used to identify mineral phases
240 and to guide subsequent quantitative analyses.

241

242 Quantitative analyses were done using the five wavelength-dispersive spectrometers and
243 a combination of diffracting crystals for two to four elements, as follows: Na, Mg, Al,
244 and Si were analyzed using the TAP crystal; Mn, Fe, and Si were analyzed using the LIF
245 crystal; Ti and Cr were analyzed using LIFH; and S, K, and Ca were analyzed using PET.
246 Elemental standards used were Amelia Albite P-103 (Na), Shankland synthetic Forsterite
247 P-658 (Mg), Alaska Anorthite NMNH 137041 (Al), Gates Wollastonite (Si and Ca),
248 Madagascar Orthoclase GRR78 (K), Mn Olivine RDS P-1087 (Mn), Fe₂O₃ Elba
249 Hematite P-238 (Fe), TiO₂ GRR (Ti), and Cr₂O₃ P-585 (Cr). Quantitative analyses were
250 done using Probe for EPMA software and x-ray corrections were done using the CITZAF
251 correction software ($\Phi(\rho z)$ algorithm; *Armstrong et al., 1995*).

252

253 Because the microprobe does not distinguish Fe^{2+} and Fe^{3+} , total Fe concentrations are
254 reported in terms of FeO. These values were converted to Fe_2O_3 for comparison with
255 bulk chemical analyses, for which total Fe was reported as Fe_2O_3 . For magnetite and
256 spinels, Fe_2O_3 values were adjusted for contributions from ferric oxide (Fe^{3+}) using
257 stoichiometry. The fraction of Fe^{3+} to total iron was calculated by adjusting the fraction
258 of Fe^{2+} to total iron until the sum of total cations was 3.00.

259

260 ***3.5 X-ray Diffraction***

261 Bulk rock powders were placed into 3.8 cm by 5 cm fixed sample mounts and tamped
262 down using a metal spatula in order to form a flat surface. X-ray diffraction (XRD)
263 measurements were taken using the Bruker d8 X-ray powder diffractometer at
264 Washington University in St. Louis using Cu-K α radiation at a maximum power of 100W
265 operating at 40 kV and 40 mA, with a 0.5 per second per step count time. Data was
266 analyzed using the DIFFRAC.EVA and DIFFRAC.SUITE TOPAS software for Rietveld
267 refinement. Rietveld refinements were performed automatically, using a peak fitting
268 algorithm with a library of standard minerals, and manually by selecting peaks of interest
269 and identifying potential mineral candidates based on bulk geochemical data.

270

271 **4.0 Results**

272 ***4.1 VSWIR spectral Analysis***

273 Diversity in spectral properties both among samples and within samples indicates
274 differences in both weathering extent and the nature of weathering chemical processes
275 affecting the rocks. For the host rock, key features were the variation in overall slope and

276 continuum shape, the depth of absorption features related to ferric iron, and the depth or
277 narrowness of vibrational absorption features at longer wavelengths (1.4 to 2.5 μm),
278 indicating the presence of metal-OH and H₂O (Table 1; Figure 3).

279 *4.1.1 Continuum shape and slope*

280 Overall continuum shape and slopes at longer wavelengths are indicators of the degree
281 of alteration, as well as the style of alteration. Less altered samples have an overall flat
282 slope with few prominent absorption features. This pattern is typical for a relatively
283 pristine basalt, which has an overall low albedo and shallow, broad features related to
284 pyroxene around 1.0 μm and 2.0 μm . With increasing alteration, the overall continuum
285 shape changes from flat to downward sloping (blue-sloped spectrum), e.g., samples B and
286 F. Blue-sloped spectra can indicate surface coatings on basalts, and a gypsum coating
287 was identified for sample F [Skok et al., 2010]. As alteration progresses, the overall
288 continuum shape becomes more curved and has a concave-down shape, common for
289 spectra of altered materials due to ferric oxide absorption at shorter wavelengths and the
290 leftward shoulder of the strong OH and H₂O absorptions from 2.7 to 3 μm . The samples I
291 and A have the most curved, concave-down overall continuum shape. Based on overall
292 continuum shape and slope, samples are ordered, in terms of increasing alteration, from J,
293 K, B, F, C, I, to A (Table 3).

294

295 *4.1.2 Fe-related absorptions*

296 Indicators of ferric iron are absorption features at 0.53 and \sim 0.9 μm , as well as slopes
297 between 0.6 and 0.8 μm . Relatively pristine basalts have shallow bands at 0.53 μm and
298 broad, shallow bands at \sim 0.9 μm , related to Fe(III) electronic transitions in crystalline Fe-

299 oxides. The depths of both of these bands are related to ferric iron content, and increase
300 with increasing alteration; sample A has a strong absorption feature at 0.53 μm and a
301 sharp band at 0.91 μm . Slopes between 0.6 and 0.8 μm also indicate the presence of Fe-
302 oxides. Samples J and K have a negative slope between 0.6 and 0.8 μm , suggesting little
303 to no ferric iron content, whereas samples I and A have steep positive slopes in this same
304 region, suggesting greater ferric iron content with increasing alteration. On the basis of
305 the band depth at 0.53 μm (BD530), samples are ordered in terms of increasing ferric iron
306 content from J, K, B, F, I, C, to A.

307

308 *4.1.3 H₂O and metal-OH absorptions*

309 Absorption features at 1.9 μm are an indicator of H₂O in clay interlayers, hydrated silica,
310 or other hydrous phases and should increase with alteration and sample weathering. In the
311 San Carlos samples, increasing BD1900 is correlated with BD530, suggesting a
312 relationship between water and ferric iron content (Figure 4). All samples contain bands
313 at 1.4 μm of varying depths, related to hydroxyls in hydrated silicates and molecular
314 water; these features are small and shallow in J and K samples, and increase in depth for
315 C, I, A samples.

316 Absorption features at longer wavelengths indicate the presence of hydrated silicates. The
317 depth and position of absorption features at longer wavelengths varies significantly
318 between samples, indicating changes in Al-OH and Fe,Mg-OH content (Table 2). Less
319 altered samples (J and K) have broad, shallow absorption features near 2.2 μm , indicating
320 Si-OH possibly due to the presence amorphous silica or poorly crystalline silicate
321 weathering products. More altered samples have sharper absorption features at 2.2 μm ,

322 indicating Al-OH and/or weak, broad features at 2.29 μm or 2.3 μm , indicating Fe or Mg-
323 OH. Sample B has a both a broad absorption feature at 2.2 μm due to Si-OH and a sharp
324 feature at 2.3 μm , indicating greater Fe/Mg-OH-bearing phase content compared to other
325 samples. Samples A and I have strong, sharp absorption features at 2.2 μm and weaker
326 bands at 2.3 μm , suggesting more crystalline Al clays, or greater Al-OH content
327 compared to Mg-OH content. BD2210 (Al-OH or Si-OH) increases with BD1900 (water
328 content) and BD530 (ferric iron content) for all samples, suggesting a trend in alteration
329 with increasing and correlated Si-OH/Al-OH and ferric iron as alteration progresses.
330 BD2290 (Fe-OH) varies little with other spectral parameters and only one sample (B) has
331 a BD2290 value above 0.03 (Table 3; Figure 4).

332

333 From the initial suite of 7 rocks, 4 spectral endmembers were identified on the basis of
334 these three classes of spectral parameters. J appears to be the least altered sample with an
335 overall flat continuum shape, weak ferric absorption features, and broad features at 2.2
336 μm . B is an intermediately altered basalt, and has a blue-sloped spectrum, a weak band at
337 0.53 μm , broad features at 2.2 μm , and a sharp feature at 2.3 μm . C is also an
338 intermediately altered basalt but with a slightly curved, concave-down continuum shape
339 and small, sharp features at 0.53 and 2.2 μm . Sample A is the most altered sample with a
340 curved, concave down overall shape and very sharp absorption features at 0.53 and 2.2
341 μm . These 4 samples represent a different extent and/or style of weathering, and their thin
342 sections were analyzed in detail with the electron microprobe.

343

344

345 ***4.2 Bulk Chemical Analysis***

346 Results from bulk chemical analysis are given in weight percent oxide for all 7 samples,
347 along with calculated normative mineralogy (Table 4). Totals range from 95.2% to 99.1%
348 with differences due to loss on ignition and slight variations in $\text{Fe}^{2+}/\text{Fe}^{3+}$. Variations in
349 weight percents for individual oxides are minimal, with the most variation in Na_2O
350 (3.34% to 5.27%). Bulk rock compositions fall within the basanite field on a TAS
351 diagram (Figure 1). Sample J has a slightly higher alkali content (7.46 %) compared to all
352 other samples. In contrast, sample Sample A, has a slightly lower alkali content (5.61 %)
353 relative to other samples. From bulk chemical data, normative mineralogy for each
354 sample was calculated by the CIPW normative method. The San Carlos samples have less
355 silica and alkalis than the Jake M rock at Gale crater (Stolper et al., 2013) and are most
356 comparable to the Wishstone class at Gusev crater (McSween et al., 2006), albeit slightly
357 lower in magnesium and iron.

358

359 ***4.3 Electron Microprobe Analysis***

360 The four spectral endmembers were analyzed using backscattered electron imaging and
361 spot analyses to look for primary and alteration textures, and determine mineral
362 compositions. Key findings were distinct textures for olivine, titanomagnetite, and
363 plagioclase laths, compositional ranges for various minerals, and evidence for alteration
364 on the micron scale.

365

366 ***4.3.1 Overall textures and mineral assemblages***

367 All samples have an overall porphyritic texture with larger olivine phenocrysts set in an
368 intergranular matrix of plagioclase laths with interstitial pyroxene, titanomagnetite, and
369 nepheline. Small amounts of glass might be present between grains, but were not detected
370 in petrographic microscope images or verified by electron microprobe analyses. For
371 sample J, most grains are euhedral and grain boundaries are well-defined, and throughout
372 the sample, the texture remains consistent (Figure 5a). The mineral assemblage consists
373 of plagioclase, high-Ca pyroxene (augite), nepheline, and titanomagnetite, with zoned
374 olivine phenocrysts. Samples B and C consist of the same mineral assemblage, with the
375 exception of zoned titanomagnetite in B, which is not present in C (Figure 5b and c). For
376 sample A, the overall texture in the interior of the section was similar to that for the
377 pristine sample; towards the rock exterior, most of the grains are subhedral, while the
378 grain boundaries are poorly defined and appear frayed or ragged (Figure 5d,e, and f). In
379 Sample B, grain boundaries at the rock exterior also appeared frayed (Figure 5g). The
380 mineral assemblage for the Sample A consists of mottled plagioclase, high-Ca pyroxene
381 (augite), nepheline, leucite, and titanomagnetite intergrown with an ulvöspinel phase,
382 with olivine phenocrysts, some of which have been partially altered to poorly crystalline
383 hematite or other iron-enriched phases (Figure 5h).

384

385 *4.3.2 Compositions by mineral*

386 Olivine phenocrysts have compositions between Fo₉₀ and Fo₆₀ (Figure 6). For sample (J)
387 olivine compositions cluster around Fo₉₀ with only a little zoning with higher Fe near the
388 rim. More altered samples contain mixtures of olivine and hematite or another iron oxide
389 from olivine alteration/oxidation. Possibly, olivine dissolution with removal of Mg²⁺ and

390 oxidation of FeO to Fe₂O₃ is responsible for the variably high iron olivines in more
391 altered rocks. Pyroxene is mostly high Ca pyroxene (Figure 7). Most compositions plot in
392 the augite field, with several compositions falling in the pigeonite and enstatite fields.
393
394 Opaque mineral compositions plot between Ti-hematite (ilmenohematite) and
395 titanomagnetite in solid solution with ulvöspinel (Figure 8). Sample J contains only
396 titanomagnetite with no ulvöspinel phase. Sample A contains a wormy intergrowth of
397 ulvöspinel and titanomagnetite partially oxidized to ilmenohematite. Sample C contains
398 pristine titanomagnetite or titanomagnetite with distinct zones of exsolved ulvöspinel.
399
400 Feldspar compositions mostly lie in the plagioclase field between An₃₀ and An₇₀ (Figure
401 9). Sample J, has an average plagioclase composition of An_{56.5}Ab₄₂Or_{1.5}. Samples B and
402 C have average compositions of An₅₀Ab₄₈Or₂ and An₄₉Ab₄₉Or₂, respectively. Sample A
403 has an average plagioclase composition of An₅₄Ab₄₄Or₂. A few compositions fall within
404 the alkali feldspar field (compositions on average are ~An₂₁Ab₆₃Or₁₆). These
405 compositions are alkali-rich edges from zoning of plagioclase in the primary melt. Both
406 samples B and C contained zoned feldspars, with the average alkali-rich rim composition
407 of An₂Ab₄₆Or₅₂ in B and An₅Ab₄₇Or₄₈ and An₅Ab₇₅Or₂₀ in C. Feldspathoids fall into two
408 groups, nepheline or leucite, and occur as distinct grains between plagioclase laths or as
409 individual grains near clusters of plagioclase laths. Nepheline is present in all samples,
410 whereas leucite only occurs in samples C and A. Leucite compositions approach
411 endmember KAlSi₂O₆, while nepheline compositions vary between samples. J has an
412 average nepheline composition of Ne₇₁Ks₆An₁Qz₂₁; Samples A, B, and C have average

413 nepheline compositions of $\text{Ne}_{68}\text{Ks}_6\text{An}_2\text{Qz}_{23}$, $\text{Ne}_{71.5}\text{Ks}_{6.5}\text{An}_{1.1}\text{Qz}_{20.6}$, and $\text{Ne}_{68}\text{Ks}_6\text{An}_{11}\text{Qz}_{14}$,
414 respectively.

415

416 Evidence of phyllosilicates is found in samples A and B (Figure 10). Phyllosilicates in
417 sample A occur between plagioclase laths, along the rims of altered olivine grains, and
418 between plagioclase and augite crystals. Most of these materials analyzed with the
419 electron microprobe have weight percent oxide totals between 80% and 89% suggesting
420 that they contain a significant amount of OH or H_2O . For sample A, the most
421 phyllosilicate-like compositions were found between plagioclase laths. In the sample B,
422 most phyllosilicate-like compositions were found around altered olivine rims or between
423 altered olivine rims and plagioclase laths. Spot analyses between plagioclase laths
424 revealed more montmorillonite-like compositions. Analyses between altered mafic
425 minerals revealed compositions similar to saponite, other Fe/Mg smectites, and chlorite
426 (Figure 10).

427

428 *4.3.3 Primary and secondary textures*

429 Primary textures for olivine phenocrysts are euhedral crystals with angular boundaries,
430 best seen in sample J. There is some zoning but compositions are overall Mg-rich (Figure
431 5a). In samples A, B, and C, olivine grains are zoned and many have a veiny texture
432 along the edges or through the grain, representing olivine altered to hematite or another
433 Fe(III) oxide (Figure 5b-h). Primary plagioclase and alkali feldspars, identified from
434 sample J, are elongated laths with well-defined grain boundaries (Figure 5a). Feldspar
435 laths in A, B, and C have a range of textures from mottled or wormy on the rock exterior

436 to fairly pristine in the rock interior (Figure 5b, c, and e). Highly irregular, wormy
437 feldspar laths are present in sample A only (Figure 5e and f). Primary augite is euhedral
438 with angular boundaries for all samples, and no alteration textures for pyroxene were
439 found. Titanomagnetite in sample J occurs as bright, distinct grains with well-defined
440 grain crystal boundaries (Figure 5a). Other samples contain pristine titanomagnetite
441 textures (C) and intergrown titanomagnetite and ulvöspinel (possibly exsolved; B)
442 (Figure 5b and c). Secondary alteration textures for titanomagnetite occur only in the
443 sample A, where titanomagnetite crystals have a mottled, wormy texture with some
444 irregularly shaped, distinct spinel zones (Figure 5e and f).

445

446 ***4.4 XRD Analysis***

447 Using both an automated peak fitting algorithm and manually selected peaks for inclusion
448 in the Rietveld refinement model, we identified mineral assemblages and the percentages
449 of each mineral for every sample. The resultant mineral suites are in agreement with the
450 assemblages identified by our normative mineralogy analysis of the bulk chemical data
451 (Figure 11a-b, Table 4). Phyllosilicate peaks were not directly detected at low-2 θ but
452 phyllosilicates identified in VSWIR spectra and microprobe images were also included in
453 Rietveld refinements.

454

455 ***4.4.1 Forward Modeling***

456 We combined the percentages of minerals identified by Rietveld refinement with the
457 average mineral compositions obtained from electron microprobe point analyses in order
458 to obtain total oxide abundances. All of the phases identified by Rietveld refinement were

459 listed, and, when available, the average composition (in terms of oxide weight
460 percentages) from electron microprobe spot analyses was assigned as the ‘true’
461 composition for each mineral. Each oxide weight percent was weighted by the percentage
462 determined through the Rietveld refinement analysis. These percentages were then
463 adjusted in order to closely match the bulk oxide weight percentages with the bulk
464 chemical analysis data, minimizing residuals (Tables 3, 4). Most of the minerals detected
465 in the XRD data set were also identified in electron microprobe images and analyzed by
466 direct spot analyses. Also, the relative order of the most abundant primary minerals in
467 XRD (arranged from most to least abundant) is in agreement with the normative
468 mineralogy calculations and visual analysis of petrographic microscope images. For the
469 primary minerals, the order from most to least abundant is: plagioclase, augite, olivine,
470 nepheline, and ulvöspinel/titanomagnetite (Table 4).

471

472 **5.0 Discussion**

473 Results from VSWIR spectra suggest multiple weathering products and evidence for the
474 formation of ferric oxides, crystalline to poorly-crystalline phyllosilicates, and
475 amorphous silica coatings or weathering products in varying amounts for all samples.
476 Results from bulk chemical analysis indicate weathering is modest and largely
477 isochemical with little changes in oxide weight percent totals between individual samples,
478 except for 1-2% alkali and silica (Figure 12a-g). Electron microprobe analysis found little
479 evidence for pervasive phyllosilicate or ferric oxide alteration, but rather distinct
480 alteration textures and relatively similar compositions for the primary minerals (feldspars,
481 pyroxene, olivine, and opaques).

482

483 ***5.1 VSWIR Spectra Weathering Trends***

484 Overall shape varies from relatively flat (relatively pristine basalt with minor coatings
485 and phyllosilicates; J) to downward sloping (presence of coatings and small amounts of
486 phyllosilicates; B) to concave down (clay-like; C and A) as alteration increases. This
487 suggests an overall trend from relatively pristine basalt to thin coatings to well-ordered
488 phyllosilicates. The band depth at 0.53 μm (BD530) and the slope between 0.6 and 0.8
489 μm increase with increasing alteration (as determined by changes in continuum shape,
490 petrographic textures, and chemistry of discrete mineral phases). This suggests an overall
491 trend in increasing ferric iron and oxidation as alteration progresses. BD1900 increases
492 with increasing sample alteration based on visual analysis (amount of red material on
493 surface) and overall continuum shape. BD1900 also correlates with both BD530 and
494 BD2210 suggesting a continuous alteration trend of increasing hydration (BD1900), iron
495 oxidation (BD530), and Si/Al-OH bearing phases (BD2210; Figure 4a, b, and c). A
496 similar overall trend is reflected in the correlation between BD2210 and BD530,
497 suggesting a trend of increasing Si/Al-OH bonds and oxidation as alteration progresses
498 (Figure 4d and e). Band depths at longer wavelengths (BD2210 and BD2290) show little
499 correlation, indicating that Fe/Mg-OH and Si/Al-OH for well-crystalline hydrated
500 silicates are not strongly related (Figure 4a). BD2290 and BD530 are also not correlated,
501 possibly indicating iron oxide formation is not closely related to the processes that create
502 Fe-OH and Mg-OH bearing phases in these samples.

503

504 ***5.2 Bulk Chemistry Weathering Trends***

505 The bulk rock samples all plot in the basanite field and have little variation in bulk
506 composition (Figure 1; Table 2). The CIA (chemical index of alteration) values for all
507 samples range from 0.526 (sample A) to 0.505 (sample J). On a classic diagram used in
508 studies of terrestrial and martian weathering (e.g., *Nesbitt & Wilson, 1992; Nesbitt &*
509 *Young, 1989*), there is little evidence for mobility of cations and chemical alteration.
510 Despite the similarity in bulk composition, some trends between silica and other oxides
511 or sums of oxides arise (Figure 12a-g). Silica and alkalis are positively correlated (Figure
512 12a), with high-alkali, high-silica compositions corresponding to the less altered samples
513 (J, K, and F) and lower-alkali, lower-silica compositions corresponding to more highly
514 altered samples (B, A, and I). A similar correlation occurs for silica and Na₂O (Figure
515 12b). CaO and silica are negatively correlated (Figure 12c); higher silica (less altered)
516 samples are lower in CaO compared to lower silica (more altered) samples ($R^2 = 0.43$).
517 This trend may be caused by preferential retention of CaO during weathering or by Ca-
518 rich fluids. The former seems favored by the lack of evidence for salts in most samples
519 (except the surface of F) and the pristine pyroxene grains observed in altered rocks.
520 Al₂O₃ and Fe₂O_{3T} are not correlated with Si (Figure 12d and e). MgO remains relatively
521 constant for all values of silica (Figure 12f). In general, for common basaltic minerals and
522 glass, glass is the first to weather, followed by olivine, pyroxene, and then plagioclase
523 [*Eggleton et al., 1987*]. The typical ion mobility relationship is Na > K > Ca > Si > Mg >
524 Al > Ti > Fe for basaltic weathering [*Gislason et al., 1996*]. Na and K are assumed to be
525 mainly released from the weathering of plagioclase. Na₂O and K₂O contents typically
526 decrease with increasing alteration, and this trend is found for these samples (Figure 12a).
527 Mg and Ca, released by weathering of olivine and pyroxene, respectively, typically

528 decrease with increasing alteration, but that is not the case for these samples. Both
529 elements are retained, along with Fe, while Si does appear to have been transported in a
530 similar manner to the alkalis. Plots of oxides vs. loss on ignition (LOI) show interesting
531 trends relating to changes in chemistry with hydration and/or oxidation (Figure 13a-c).
532 LOI is strongly inversely correlated with silica content (Figure 13a); lower LOI values
533 correspond to higher silica values (less altered samples ($R^2 = 0.76$). A similar inverse
534 correlation occurs between LOI and alkali content (Figure 13b), suggesting that more
535 altered samples (A, B, and I) have higher LOI values and lower alkali content compared
536 to less altered samples ($R^2 = 0.58$). CaO and LOI are positively correlated (Figure 13c),
537 with more altered samples having high LOI and high CaO compared to less altered
538 samples ($R^2 = 0.61$). In these samples, we infer that the most mobile cations were (in
539 order of decreasing mobility) Na, K, Si, Fe, Mg, Ca, and Al. The lack of weathering of
540 pyroxene appears essential for these trends.

541

542 Comparison of oxides to spectral parameters shows similar trends as oxide-oxide plots.
543 BD1900 negatively correlates with alkali content, suggesting a relationship between
544 increasing hydrous alteration and decreasing alkali content due to cation mobility (Figure
545 14a-d). However, BD1900 is not correlated with Fe_2O_{3T} ($R^2 = 0.03$). Some more altered
546 (higher BD1900) samples are preferentially enriched in Fe_2O_{3T} , potentially due to the
547 formation of Fe(III) oxides observed in Samples A, B, and C. Sample C is anomalous in
548 that it has relatively high Fe_2O_{3T} , but BD1900 is low compared to all samples (Figure
549 14d). Similar trends found in silica and BD1900 plots are seen in comparisons of BD530
550 with alkalis (Figure 15a). Alkali content generally decreases with increasing BD530; this

551 trend is controlled by the strong negative correlation between BD530 and Na₂O, due to
552 the mobility of Na in basaltic weathering pathways. BD530 shows a strong positive
553 correlation with Fe₂O_{3T}, and band depth increases with increasing Fe₂O_{3T} content (Figure
554 15c). Both BD1900 and BD530 show a positive correlation with CaO, possibly due to the
555 lack of weathering of Ca-rich pyroxenes (Figures 14b and 15d).

556

557 ***5.3 Electron Microprobe Mineralogical Analyses of Alteration***

558 On the basis of point analyses and traverses of individual grains, alteration processes
559 were found to affect individual minerals differently, adding context to the general
560 weathering patterns given by VSWIR spectra and bulk chemistry. Most minerals
561 identified by VSWIR spectra were verified by microprobe data; hematite, Al smectite,
562 Fe/Mg phyllosilicates, olivine, and high-Ca pyroxene were all identified through BSE
563 imaging and spot analyses.

564

565 For olivine grains, edges were altered to ‘veiny’ textures composed of hematite or
566 another Fe(III) oxide like goethite or ferrihydrite. Highly altered olivine grains were
567 transformed into a ‘mesh’ of hematite (or other Fe(III) oxide) veins, with only small areas
568 of Fe(II)-rich olivine remaining. Primary olivine grains are unzoned in the least altered
569 sample (J), and olivine phenocrysts in altered samples (A, B, and C) have magnesian
570 cores. Olivine grains in altered samples have rims that are higher in Fe owing to primary
571 compositional zoning or oxidation to hematite; hematite alteration is indicated by a
572 vermicular texture on the olivine grain rim. Analyses show both compositional zoning
573 (Fe-rich rims vs. Mg-rich cores) and mixing of olivine with altered hematite veins (Figure

574 6). There is no silica directly (spatially) related with this alteration, thus it appears that
575 silica was mobile and lost from the grain, as was Mg, though these elements were not
576 always clearly lost from the bulk sample. Two traverses across larger olivine grains in J
577 and C also found olivine-pyroxene intergrowths. Pyroxene was found to vary little; most
578 compositions plot in the augite field (average composition of $Wo_{39}En_{48}Fs_{13}$) and
579 alteration textures similar to those for olivine were not observed, indicating this phase
580 was not susceptible to alteration [as also observed by *Eggleton et al.*, 1987].
581
582 Typical feldspar compositions for J, A, and C fall within a plagioclase composition
583 (between An_{30} and An_{70}). Analyses in sample B found alkali-rich rims (average
584 composition $An_2Ab_{46}Or_{52}$) along the edges of plagioclase laths reflecting overgrowth of
585 plagioclase grains by material precipitated from evolved residual melt (Figure 9). Mottled
586 textures were found for many feldspar laths in A, B, and C, and alkali-rich feldspars
587 (average compositions $An_5Ab_{47}Or_{48}$ and $An_5Ab_{75}Or_{20}$) were detected on lath edges in
588 sample C (Figure 5). More pristine feldspar samples have higher anorthite components,
589 and overall higher amounts of Ca, while more altered samples have more alkali-rich
590 compositions. All samples contain dark, unaltered phases between plagioclase laths,
591 consistent with nepheline compositions. Smaller laths of leucite are also present in A and
592 C.
593
594 Opaque phases were found as discrete grains of titanomagnetite and intergrowths of both
595 titanomagnetite and ulvöspinel. This latter occurrence may be the result of exsolution of
596 ulvöspinel as samples are altered [*Price*, 1980]. Alternatively, the ulvöspinel and

597 titanomagnetite intergrowth could be a primary texture from cooling or changes in
598 oxygen fugacity of the original lava. For example, ulvöspinel and titanomagnetite exist as
599 one phase at high temperatures; as temperature decreases, ulvöspinel exsolves out as a
600 separate phase. Textures of the zoning are irregular and amoeboid-like for the most
601 altered sample (A), and angular/well-defined for less altered samples (B and C). No
602 zoning was observed in the least altered sample (J), all opaques were titanomagnetite. In
603 addition to zoning, titanomagnetite altered to ilmenohematite, indicating increased
604 oxidation (Figure 8). Phyllosilicate clay alteration was not pervasive, and most
605 measurements of potential clay minerals were limited to a few micrometers distance from
606 the edges of the plagioclase laths or altered olivine. Highly altered phases with frayed
607 edges in the interstices between feldspar laths, around olivine edges, and in vesicles are
608 likely poorly ordered phyllosilicates. Weight percent totals for most of the inferred
609 phyllosilicates were low, between 80 and 90 %, consistent with 10 to 20 percent water
610 contents, typical for many smectites. Ternary diagrams of Al, Fe, and Mg, common
611 cations in smectite octahedral sites, show most phyllosilicate-like materials in sample A
612 plotting near the Al vertex, near montmorillonite. Phyllosilicate-like compositions in
613 sample B fall between Mg and Fe, suggesting trioctahedral smectites (Figure 10).

614

615 ***5.4 Possible Alteration Pathways***

616 Overall alteration trends, as opposed to distinct weathering pathways, are suggested by
617 bulk chemical data and comparison of oxides with spectral parameters (Figure 16; Figure
618 17a). Comparisons of BD1900 and BD2210 suggest an alteration pathway from J to C
619 and A, characterized by a change from amorphous silica to Al-smectites with greater

620 hydration of feldspars and accompanying formation of Fe-oxides from olivine, ulvospinel,
621 and titanomagnetite. Comparison of BD2210 and BD530 suggests an overall alteration
622 trend related to increasing amorphous silica and/or well-ordered Al-phyllsilicates, as
623 well as oxidation.

624 BD2290 shows no correlation with BD1900 ($R^2=0.0054$) when considering all samples,
625 however, Sample B has a large BD2290 value compared to all other samples. This
626 indicates that Sample B might represent the early stages of alteration, where only the
627 most susceptible mineral, olivine, is dissolved to form Fe/Mg-phyllsilicates. Alteration
628 may not have been pervasive enough in Sample B to also form Al-phyllsilicates, like
629 those present in Samples A and C. Thus, Sample B, compared to Samples A and C, might
630 be a less weathered example of the same alteration pathway that formed Samples A and
631 C. Alternatively, Sample B might represent an alternate weathering regime where Fe
632 from dissolved olivine is preferentially incorporated into phyllsilicates, and Fe is not
633 oxidized to form hematite or other Fe(III) oxides (Figure 12d).

634

635 The trend of decreasing alkalis with decreasing silica in feldspars emphasizes the direct
636 relationship in bulk chemical compositions, and suggests something about cation
637 mobility as these samples are altered. It is possible that decreasing alkali content in the
638 bulk composition is related to the weathering of plagioclase grains as alteration
639 progresses (Figure 17b). Increasing Ca with increasing silica content in the bulk
640 composition may be caused by retention of Ca due to the lack of pyroxene alteration, as
641 other primary phases are weathered. LOI (as a measure of sample hydration) is negatively
642 correlated with alkali and SiO₂ content, and confirms the trend of increasing hydration (as

643 measured by B1900) with decreasing alkali and SiO₂, related to the loss of alkalis due to
644 the weathering of feldspars as alteration progresses.

645 Data from the electron microprobe indicates increasing oxidation, loss of alkalis (Na and
646 K), and the formation of Al-OH and/or Fe/Mg-OH phyllosilicates as samples are altered
647 (Figure 17c). The wormy intergrowths of titanomagnetite and ulvöspinel in the most
648 altered sample (A) contain ilmenohematite from the oxidation of titanomagnetite. Further
649 evidence for persistent iron oxidation is indicated by Fe(III) oxide rims or a ‘mesh’ of
650 Fe(III) oxide veins in olivine grains for altered samples (A, B, and C). Fe²⁺, concentrated
651 in the rims of zoned olivine grains, is oxidized to Fe³⁺ as alteration progresses. Olivine
652 grain rims, then, are preferentially altered to poorly crystalline hematite (or other Fe(III)
653 oxide), as evidenced by the veiny ‘mats’ of poorly crystalline Fe(III) oxide on olivine
654 rims in B and A. As alteration progresses, the Fe-rich rims of olivine grains are
655 completely altered to a pseudo-hematite phase and orange-colored veins pervade through
656 the Mg-rich olivine core. Mottled plagioclase laths in altered samples indicate some
657 alteration of plagioclase, which may relate to decreasing alkali content trends seen in the
658 bulk chemical data. Frayed grains along the edges of plagioclase laths may represent
659 phyllosilicates formed from plagioclase alteration (Figure 10). Weathering of plagioclase
660 releases alkalis (Na and K), Ca, Al, and Si. Most of the alkalis are lost, resulting in the
661 general trend of decreasing alkali content relative to Si; however, it is possible that some
662 K is incorporated with Al into leucite (KAlSi₂O₆), as leucite is only present in altered
663 samples A, B, and C. Al and Si are retained, and likely incorporated into phyllosilicates
664 along the edges of mottled plagioclase laths, resulting in the relative immobility of Al
665 compared to Si seen in bulk chemical data. Compositions for these grains plot near the Al

666 vertex of the Al-Fe-Mg diagram, verifying the Al-rich phyllosilicate signatures seen in
667 VSWIR spectra for two of the altered samples (A and C). Si and Mg are lost as the more
668 Mg-rich olivine is dissolved, and incorporated into the Fe/Mg phyllosilicates found along
669 the edges of altered olivine grains in B. Analyses for frayed grains along the edge of
670 altered olivine grains plot along the Mg-Fe join, verifying spectral data of saponite or
671 other Fe/Mg phyllosilicates. Thus, Al clays are likely created by the alteration of
672 plagioclase laths, while Fe/Mg phyllosilicates are formed from altered Mg-rich olivine
673 [as also seen by *Velde & Nicot*, 1985]. The Fe-rich rims of the zoned olivine are oxidized
674 to form pervasive pseudo-hematite veins, and titanomagnetite is also oxidized to form
675 ilmenohematite, causing ulvöspinel to exsolve out as a secondary phase. Pyroxene and
676 nepheline, both present in unaltered sample, J, and persistent in all altered samples,
677 remain pristine and show no signs of alteration (Figure 17d).

678

679 **6.0 Implications**

680 In the context of recent discoveries on Mars by MER and MSL, it is evident that alkaline
681 basaltic rocks are present on Mars, and their primary mineralogy, as well as any alteration
682 products, needs to be further studied [*McSween et al.*, 2006; *Stolper et al.*, 2013]. The San
683 Carlos suite of high-alkali basalts (basanites), studied here, with moderately high alkali
684 percentages and feldspathoid phases is particularly relevant as an analog. VSWIR
685 spectral analyses detected metal-OH absorptions and Fe(III) electronic transitions of
686 secondary minerals formed by hydrous alteration and oxidation. Signs of hydration and
687 oxidation are also seen in bulk chemical data in the San Carlos suite as trends of various
688 oxides versus LOI or silica; however, both bulk chemistry and electron microprobe

689 analyses show that samples have undergone mainly isochemical alteration, with only
690 subtle compositional variations accompanying alteration in Na, K, and Si (Figure 16).
691 XRD analyses provide identification and structural information on the primary phases
692 within samples. They are sometimes sensitive to the presence of clays and other
693 amorphous substances, but did not identify the small amounts of clays observed here with
694 the other techniques. Electron microprobe microanalysis reveals the effects of oxidation
695 and also that the development of phyllosilicate clay minerals is subtle. BSE images of
696 alteration textures showed altered mineral phases indicated by VSWIR data, and spot
697 analyses also revealed the effects and extent of oxidation. Areas around the edges of
698 wormy plagioclase laths and oxidized olivine grains were found to contain phyllosilicate-
699 like compositions, corresponding to the phyllosilicate identifications from the spectral
700 data. Evidence for the oxidation of iron (Fe^{2+} to Fe^{3+}) is also evident in analyses of
701 mottled titanomagnetite and ulvöspinel intergrowths in the most altered sample (A).
702 Alteration was most prevalent within a few millimeters of the sample's surface. The
703 samples still contain mostly primary mineralogy with some incipient alteration.

704

705 The nature of alteration observed here over the last 2-3 Ma for the San Carlos alkaline
706 basalts is similar to results from some studies of subalkaline basalts. Salvatore et al.
707 [2013] found limited formation of crystalline products in oxidative weathering rinds of
708 basalts from Antarctica, and Ehlmann et al. [2012] found evidence for mostly closed-
709 system alteration in basalts in contact with Icelandic groundwater systems. In contrast,
710 Greenberger et al. [2012] found mostly open system weathering in Deccan traps basalts.
711 The main controls on alteration style and secondary mineralogy appear to be time,

712 temperature, and the activity of H₂O. In this way, San Carlos is intermediate in alteration
713 extent between the Antarctica samples analyzed by Salvatore and the Icelandic samples
714 analyzed by Ehlmann. San Carlos samples show less evidence for well-crystalline
715 alteration products, but have similar spectral signatures to the Icelandic samples analyzed
716 by Ehlmann. The presence of additional alkalis does not appear to appreciably change the
717 secondary mineralogy. As expected from prior work [e.g. *Nesbitt and Wilson*, 1992], the
718 alkalis are most readily mobilized. They are one of the few elements with measurable
719 chemical trends here. Aiuppa et al. [2000] inferred the dissolution susceptibility of
720 primary minerals to be olivine > clinopyroxene > plagioclase in alkaline basalts altered
721 by CO₂-rich groundwater, though here we found olivine > plagioclase > pyroxenes.
722
723 Formation of Fe(III)-bearing oxides, silica, and/or Al/Fe/Mg phyllosilicates is similar to
724 mineral assemblages observed on Mars at multiple locations. Al smectites, Fe/Mg
725 smectites, Fe oxides, and hydrated silica have been identified in multiple locations [e.g.,
726 *Ehlmann & Edwards*, 2014]. Nearly isochemical alteration during oxidation and
727 hydration, as observed in San Carlos samples, seems to be typical of several formations
728 on Mars showing evidence of alteration [e.g., *Ming et al.*, 2008; *Ehlmann et al.*, 2011;
729 *McLennan et al.*, 2014] – albeit with several notable exceptions for particular rock
730 formations where leaching is more extensive [e.g. *Clark et al.*, 2007b; *Arvidson et al.*,
731 2014; *Hurowitz et al.*, 2016]. There are some differences between the primary chemistry
732 and mineralogy of our samples versus martian ones. For example, our samples have less
733 magnesium and iron than some martian alkaline basalts, and nepheline and leucite have
734 not yet been identified on Mars. Perhaps most significantly, the altered San Carlos rocks
735 have fewer amorphous phases than reported by CheMin for all rock and sand samples at

736 Gale crater so far [e.g. *Treiman* et al., 2014; *Bish* et al., 2014]. If the amorphous phase(s)
737 are secondary products of alteration (rather than primary volcanic or impact glass), this
738 may be a result of the faster reaction kinetics at warmer San Carlos, Arizona, facilitating
739 the formation of Fe oxides and phyllosilicates. Yet, these Fe oxides and phyllosilicates
740 products in the San Carlos rocks were apparently undetectable with XRD, instead being
741 revealed by a combination of VSWIR spectroscopy and electron microprobe chemical
742 analyses. This is likely because they are not yet well-crystalline on the scales being
743 probed by x-rays, and they are relatively low in abundance. One possibility is that
744 martian sedimentary rocks at Gale crater are actually more altered (bulk percent alteration
745 products) but to alteration products equally or less well-crystalline than those in our San
746 Carlos rocks. Further sampling of materials at the Gale crater site and investigations with
747 future, different payload suites are required to investigate this hypothesis.

748

749 The use of a variety of techniques elucidates the sensitivity of each method to alteration
750 products (clays and Fe oxides), primary mineralogy, and alteration styles/extent.
751 VSWIR's sensitivity to hydrated silicates is apparent in this study, where the most altered
752 sample showed sharp, deep absorptions beyond 2.2 μm , indicating the presence of silica
753 and/or montmorillonite, even in relatively "pristine" samples. Analysis with the electron
754 microprobe suggests that alteration was most pervasive on the outer surface, but evidence
755 of weathering and dissolution was visibly apparent throughout the sample. For the XRD
756 data, primary minerals (plagioclase, alkali feldspars, nepheline, augite, and
757 titanomagnetite) were easily detected and the relative abundances reflected those
758 determined from visual analysis in petrographic microscopes and backscattered electron

759 microprobe images. Secondary minerals, such as phyllosilicates and ferric oxides, were
760 identified in all samples in the spectra, but low abundances meant precise amounts were
761 difficult to determine with microprobe or XRD. Combined with VSWIR data from orbit
762 or ChemCam analyses from the first few microns of a sample, XRD provides primary
763 mineralogy and detection of well-crystalline alteration minerals and abundant amorphous
764 phases. VSWIR's sensitivity to alteration products, including the ability to identify iron
765 oxides and the major cation in phyllosilicates, even when poorly crystalline, is a useful
766 complement to primary mineralogy abundances determined from more intensive
767 geochemical methods.

768

769 Thus this study demonstrates that the existence of evidence of aqueous alteration, its
770 extent/style, and weathering pathways can be better understood using multiple techniques.
771 Bulk geochemistry was useful, in this work, for determining that alteration was mainly
772 isochemical and that cation exchanges occurred in a closed system, with the exception of
773 alkali and silica loss. This finding has important implications for Alpha Particle X-ray
774 Spectroscopy (APXS) on MER, as bulk chemistry plots provide insight on the mobility of
775 cations compared to typically immobile cations, and aid in understanding alteration styles.
776 The presence of iron oxides is an important indicator of alteration style and oxidation
777 extent, and the MER instruments had this capability with Mössbauer spectrometers,
778 though MSL does not. For the Mars-2020 rover mission with SuperCam (Raman, LIBS,
779 VSWIR), Scanning Habitable Environments with Raman & Luminescence for Organics
780 and Chemicals (SHERLOC), Planetary Instrument for X-ray Lithochemistry (PIXL),
781 combined spectroscopy and geochemistry techniques will be critical [*Maurice et al., 2015*;

782 *Allwood et al., 2015; Beegle et al., 2014*]. PIXL and SHERLOC will not be able to
783 replace the capabilities of microprobe spot analyses of individual grains, but for sand-
784 sized and larger grains, it might be possible to determine differences in weathering
785 textures and primary and secondary mineral assemblages even within phases. The
786 detection of phyllosilicates and ferric iron may be challenging, depending on specific
787 instrument sensitivities at the sub-pixel level. SuperCam SWIR spectroscopy (1.3 to 2.6
788 um) combined with SuperCam passive VNIR spectroscopy and Mastcam-Z (0.4-1.0 um)
789 multispectral imaging will be crucial for recognizing slightly aqueously altered rock
790 outcrops and mapping subtle trends, as demonstrated here.

791

792 Given the identification of primary mineralogy and alkaline composition in many rocks at
793 Gale crater by MSL, the San Carlos suite constitutes a useful terrestrial analog in terms of
794 both primary and secondary alteration mineralogy. The use, in this work, of combined
795 spectroscopy and geochemistry methods serves as a proof of concept for the importance
796 of complementary methods in both current and future missions. The implications of this
797 work have special relevance for Mars2020, and will motivate the use of instruments on
798 MER and MSL to better understand aqueous alteration on Mars.

799

800 **Acknowledgements**

801 Many thanks to Dr. Raymond Arvidson for guidance and Paul Carpenter for invaluable
802 help using the electron microprobe and X-ray diffractometer. This work was partially
803 funded by an MSL Participating Scientist grant to Bethany Ehlmann and the Caltech
804 Summer Undergraduate Research Fellowship provided programmatic support to Bryné

805 Hadnott. Use of the Bruker d8 Advance X-ray diffractometer in Earth and Planetary
806 Sciences at Washington University in St. Louis is supported by the National Science
807 Foundation, award no. NSF EAR-1161543.

808

809

810

811

812

813

814

815

816

817

818

819

820

821

822

823

824

825

826

827

828

829

830

831

832

833

834

835

836

837

838

839

840

841

842

843 **References**

844 Aiuppa, A., Allard, P., D'Alessandro, W., Michel, A., Parello, F., Treuil, M., and
845 Valenza, M. (2000), Mobility and fluxes of major, minor and trace metals during basalt
846 weathering and groundwater transport at Mt. Etna volcano (Sicily), *Geochimica et*
847 *Cosmochimica Acta*, 64(11), 1827-1841.

848

849 Allwood, A., et al. (2015), Texture-specific elemental analysis of rocks and soils with
850 PIXL: The Planetary Instrument for X-ray Lithochemistry on Mars 2020, Aerospace
851 Conference, 2015 IEEE, 1-13.

852

853 Armstrong, J. T. (1995), CITZAF: A package of correction programs for the quantitative
854 electron microbeam x-ray analysis of thick polished materials, thin films, and particles.
855 *Microbeam Analysis*, 4, 177-200.

856

857 Arvidson, R. E., et al. (2014), Ancient aqueous environments at Endeavour crater, Mars,
858 *Science*, 343(6169), 1248097.

859

860 Beegle, L. W., et al. (2014), SHERLOC: Scanning habitable environments with raman &
861 luminescence for organics & chemicals, an investigation for 2020, AGU Fall Meeting
862 Abstracts, 1, 6.

863

864 Bibring, J.P., et al. (2006), Global mineralogical and aqueous Mars history derived from
865 OMEGA/Mars Express data, *Science*, 312(5772), 400-404.

- 866 Bish, D., et al. (2014), The first X-ray diffraction measurements on Mars, *IUCrJ*, 1(6),
867 514-522.
- 868
- 869 Bishop, J. L., Pieters, C.M., and Edwards, J.O. (1994), Infrared spectroscopic analyses on
870 the nature of water in Montmorillonite, *Clays and Clay Minerals*, 42(6), 702-714.
- 871
- 872 Bishop, J.L., Lane, M.D., Dyar, M.D., and Brown, A.J. (2008), Reflectance and emission
873 spectroscopy study of four groups of phyllosilicates: smectites, kaolinite-serpentines,
874 chlorites, and micas, *Clay Minerals*, 43, 35-54.
- 875
- 876 Blaney, D. L., Wiens, R. C., Maurice, S., Clegg, S. M., Anderson, R. B., Kah, L. C., &
877 Madsen, M. B. (2014), Chemistry and texture of the rocks at Rocknest, Gale Crater:
878 Evidence for sedimentary origin and diagenetic alteration. *Journal of Geophysical*
879 *Research: Planets*, 119(9), 2109-2131.
- 880
- 881 Clark, R. N., King, T.V.V., Klejwa, M. and Swayze, G.A. (1990), High spectral
882 resolution reflectance spectroscopy of minerals, *Journal of Geophysical Research*, 95(B8),
883 12, 653-12, 680.
- 884
- 885 Clark, R.N., Swayze, G.A., Wise, R., Livo, E., Hoefen, T., Kokaly, R., Sutley, S.J.
886 (2007a), USGS digital spectral library splib06a: U.S. Geological Survey, Digital Data
887 Series 231, <http://speclab.cr.usgs.gov/spectral.lib06>.

- 888 Clark, B. C., et al. (2007b), Evidence for montmorillonite or its compositional equivalent
889 in Columbia Hills, Mars, *Journal of Geophysical Research: Planets*, 112(E6).
890
- 891 Clegg, SM, Wiens, R.C., Barefield, J.E., Sklute, E. and Dyar. M.D. (2009), Quantitative
892 remote laser induced breakdown spectroscopy by multivariate analysis, *Spectrochimica*
893 *Acta Part B*, 64, 79–88.
894
- 895 Clegg S.M., Anderson R.B., Forni O., Lasue J., Dyar M.D., Morris R.V., Ehlmann B.L.,
896 McLennan S.M., Bender S., Cousin A., Gasnault O., Martinez R., McInroy R., Melikechi
897 N., Meslin P.-Y., Ollila A., Tokar R.L., Maurice S., and Wiens R.C. (2014), Expansion of
898 the ChemCam calibration database. *Lunar Planetary Science XLV*, 2378.
899
- 900 Clegg S.M., Wiens R.C., Anderson R.B., Forni O., Frydenvang J., Lasue J., Pilleri A.,
901 Payre V., Boucher T., Dyar M.D., McLennan S.M., Morris R.V., Graff T.G., Mertzman
902 S.A., Ehlmann B.L., Bender S.C., Tokar R.L., Belgacem I., Newsom H., McInroy R.E.,
903 Martinez R., Gasda P., Gasnault O., and Maurice S. (2016) Recalibration of the Mars
904 Science Laboratory ChemCam instrument with an expanded geochemical database.
905 *Spectrochim. Acta B*, in review.
906
- 907 Cousin, A. et al (2015), Igneous Rock Classification at Gale (Sols 13–800). *Lunar*
908 *Planetary Science Conference*, Abstract 2452.
909

- 910 Eggleton, Richard A., Foudoulis, Chris, and Varkevisser, Dane (1987), Weathering of
911 basalt: changes in rock chemistry and mineralogy, *Clays and Clay Minerals*, 35.3, 161-
912 169.
- 913
- 914 Ehlmann, B.L. and Edwards, C.S. (2014), Mineralogy of the martian surface. *Annual*
915 *Reviews of Earth and Planetary Science* 42, 291–315.
- 916
- 917 Ehlmann, B.L., Bish, D.L., Ruff, S. and Mustard, J.F. (2012), Mineralogy and chemistry
918 of altered Iceland basalts: application to clay mineral detection and understanding
919 aqueous environments on Mars, *Journal of Geophysical Research*, 117(E11).
- 920
- 921 Ehlmann, B.L., et al. (2013), An expanded training set for processing MSL ChemCam
922 LIBS data: spectral library samples added and effects on elemental compositional results
923 from Mars, *Lunar and Planetary Science XXXIV*.
- 924
- 925 Farrand, W.H., Bell III, J.F., Johnson, J.R., Squyres, S.W., Soderblom, J. and Ming, D.W.
926 (2006), Spectral variability among rocks in visible and near-infrared multispectral
927 Pancam data collected at Gusev crater: examinations using spectral mixture analysis and
928 related techniques, *Journal of Geophysical Research*, 111, E02S15.
- 929
- 930 Frey, Frederick A. and Prinz, Martin (1978), Ultramafic inclusions from San Carlos,
931 Arizona: Petrologic and geochemical data bearing on their petrogenesis, *Earth and*
932 *Planetary Science Letters*, 38(1), 129-176.

- 933 Gellert, R., et al. (2013), Initial MSL APXS activities and observations at Gale Crater,
934 Mars, Lunar and Planetary Science XXXIV.
935
- 936 Gisslason, SR, Arnorsson, S, and Armannsson, S. (1996), Chemical weathering of basalt
937 in Southwest Iceland: Effects of runoff, age of rocks, and vegetation/glacial cover.
938 American Journal of Science, 296, 837-907.
939
- 940 Golden, D. C., Ming, D. W., Morris, R. V. and Mertzman, S.A. (2005), Laboratory-
941 simulated acid-sulfate weathering of basaltic materials: Implications for formation of
942 sulfates at Meridiani Planum and Gusev crater, Mars, Journal of Geophysical Research,
943 110, E12S07,
944
- 945 Greenberger, R. N., Mustard, J. F., Kumar, P. S., Dyar, M. D., Breves, E. A. and Sklute,
946 E.C. (2012), Low temperature aqueous alteration of basalt: Mineral assemblages of
947 Deccan basalts and implications for Mars, Journal of Geophysical Research, 117, E00J12.
948
- 949 Grotzinger, J. P., Crisp, J. A., & Vasavada, A. R. (2015). Curiosity's Mission of
950 Exploration at Gale Crater, Mars. Elements, 11(1), 19-26.
951
- 952 Hausrath, E. M., Navarre-Sitchler, A. K. , Sak, P. B. , Steefel, C. I. and Brantley, S. L.
953 (2008), Basalt weathering rates on Earth and the duration of liquid water on the plains of
954 Gusev Crater, Mars, Geology, 36(1), 67–70.
955

956 Hurowitz, J. A., McLennan, S.M., Lindsley, D. H.,and Schoonen, M. A. A. (2005),
957 Experimental epithermal alteration of synthetic Los Angeles meteorite: Implications for
958 the origin of martian soils and identification of hydrothermal sites on Mars, Journal of
959 Geophysical Research, 110, E07002.

960

961 Hurowitz, J. A. and McLennan, S. M. (2007), A~ 3.5 Ga record of water-limited, acidic
962 weathering conditions on Mars, Earth and Planetary Science Letters, 260(3), 432-443.

963

964 Hurowitz, J. A., et al. (2016), Dynamic geochemical conditions recorded by lakebed
965 mudstones in Gale Crater, Mars, Lunar and Planetary Science XXXXVII.

966

967 Maurice, S. et al. (2012), The ChemCam instruments on the Mars Science Laboratory
968 (MSL) rover: science objectives and mast unit, Space Science Reviews, 170 95–166.

969

970 Maurice, S., et al. (2015), The SuperCam Instrument for the Mars2020 Rover, European
971 Planetary Science Congress 2015, 10,185.

972 McLennan, S. M., et al. (2014), Elemental geochemistry of sedimentary rocks at
973 Yellowknife Bay, Gale crater, Mars, Science, 343(6169), 1244734.

974

975 McSween, H. Y., et al. (2006), Alkaline volcanic rocks from the Columbia Hills, Gusev
976 crater, Mars, Journal of Geophysical Research, 111, E09S91.

977

978 Meslin, P.-Y. et al. (2013), Soil diversity and hydration as observed by ChemCam at Gale
979 Crater, Mars. *Science*, 341.
980
981 Milliken, R.E. and Mustard, J.F. (2005), Quantifying absolute water content of minerals
982 using near-infrared reflectance spectroscopy, *Journal of Geophysical Research*, 110,
983 E12001.
984
985 Ming, D. W., et al. (2008), Geochemical properties of rocks and soils in Gusev crater,
986 Mars: Results of the Alpha Particle X-ray Spectrometer from Cumberland Ridge to Home
987 Plate, *Journal of Geophysical Research: Planets*, 113(E12).
988
989 Minitti, M. E., Weitz, C. M., Lane, M. D., & Bishop, J. L. (2007), Morphology,
990 chemistry, and spectral properties of Hawaiian rock coatings and implications for Mars,
991 *Journal of Geophysical Research: Planets*, 112(E5).
992
993 Morris, R. (2000), Mineralogy, composition, and alteration of Mars Pathfinder rocks and
994 soils: Evidence from multispectral, elemental, and magnetic data on terrestrial analogue,
995 SNC meteorites, and Pathfinder samples, *Journal of Geophysical Research*, 105(E1),
996 1757-1817.
997
998 Mustard, J. F., et al. (2005), Olivine and pyroxene diversity in the crust of Mars, *Science*,
999 307, 1594–1597.
1000

- 1001 Mustard, J.F., Murchie, S. L. Murchie, Pelkey, S.M., Ehlmann, B.L., Milliken, R.E.,
1002 Grant, J.A., Bibring, J.P., Poulet, F., Bishop, J., Dobrea, E. Noe, Roach, L., Seelos, F.,
1003 Arvidson, R.E., Wiseman, S., Green, R., Hash, C., Humm, D., Malaret, E., McGovern,
1004 J.A., Seelos, K., Clancy, T., Clark, R., Des Marais, D., Izenberg, N., Knudson, A. (2008),
1005 Hydrated silicate minerals on Mars observed by the Mars Reconnaissance Orbiter
1006 CRISM instrument, *Nature*, 454,305-309.
1007
1008 Nesbitt, H. W., & Wilson, R. E. (1992), Recent chemical weathering of basalts, *American*
1009 *Journal of Science*, 292(10), 740-777.
1010
1011 Nesbitt, H.W. and Young, G.M. (1989), Formation and diagenesis of weathering profiles,
1012 *The Journal of Geology*, 97(2), 129-147.
1013
1014 Pelkey, S. M., et al. (2007), CRISM multispectral summary products: Parameterizing
1015 mineral diversity on Mars from reflectance, *Journal of Geophysical Research: Planets*,
1016 112(E8).
1017
1018 Price, G.D. (1980), Exsolution microstructures in titanomagnetites and their magnetic
1019 significance, *Physics of the Earth and Planetary Interiors*, 23,2-12.
1020
1021 Rogers, A. D. and Christensen, P.R. (2007), Surface mineralogy of martian low-albedo
1022 regions from MGS-TES data: Implications for upper crustal evolution and surface
1023 alteration, *Journal of Geophysical Research*, 112, E01003.

1024

1025 Salvatore, M.R. et al. (2013), Development of alteration rinds by oxidative weathering
1026 processes in Beacon Valley, Antarctica, and implications for Mars, *Geochimica et*
1027 *Cosmochimica Acta*, 115 137–161.

1028

1029 Sautter, V., et al. (2014), Igneous mineralogy at Bradbury Rise: The first ChemCam
1030 campaign at Gale crater, *Journal of Geophysical Research: Planets*, 119.

1031

1032 Sautter, V., et al. (2015), In situ evidence for continental crust on early Mars. *Nature*
1033 *Geoscience*, 8(8), 605-609.

1034

1035 Schmidt, M. E., et al. (2014), Geochemical diversity in first rocks examined by the
1036 Curiosity Rover in Gale Crater: Evidence for and significance of an alkali and
1037 volatile-rich igneous source, *Journal of Geophysical Research: Planets*, 119(1), 64-81.

1038

1039 Skok, J. R., Mustard, J. F., Ehlmann, B. L., Milliken, R. E., & Murchie, S. L. (2010),
1040 Silica deposits in the Nili Patera caldera on the Syrtis Major volcanic complex on Mars,
1041 *Nature Geoscience*, 3(12), 838-841.

1042

1043 Stolper, E. M., et al. (2013), The petrochemistry of Jake_M: A martian mugearite,
1044 *Science*, 341(6153), 1239463 .

1045

1046 Sunshine, J.M. and Pieters, C.M. (1993), Estimating modal abundances from the spectra
1047 of natural and laboratory pyroxene mixtures using the Modified Gaussian Model, Journal
1048 of Geophysical Research, 98, E5.

1049

1050 Treiman, A. H., et al. (2014), Ferrian saponite from the Santa Monica Mountains
1051 (California, USA, Earth): Characterization as an analog for clay minerals on Mars with
1052 application to Yellowknife Bay in Gale Crater, American Mineralogist, 99(11-12), 2234-
1053 2250.

1054

1055 Udry, A., Balta, J. B., & McSween, H. Y. (2014), Exploring fractionation models for
1056 martian magmas, *Journal of Geophysical Research: Planets*, 119(1), 1-18.

1057

1058 Vasavada, A. R., Grotzinger, J. P., Arvidson, R. E., Calef, F. J., Crisp, J. A., Gupta, S., ...
1059 & Yingst, R. A. (2014), Overview of the Mars Science Laboratory mission: Bradbury
1060 landing to Yellowknife Bay and beyond, *Journal of Geophysical Research: Planets*,
1061 119(6), 1134-1161.

1062

1063 Velde, B. and Nicot, E. (1985), Diagenetic clay mineral compositions as a function of
1064 pressure, temperature, and chemical activity, *Journal of Sedimentary Petrology*, 55(4),
1065 541-547.

1066

1067 Wiens, R. C., et al. (2012), The ChemCam instruments in the Mars Science Laboratory
1068 (MSL) Rover: Body unit and combined system performance, Space Science Reviews,
1069 170, 167–227.

1070

1071 Wiens, RC et al. (2013), Pre-flight calibration and initial data processing for the
1072 ChemCam laser-induced breakdown spectroscopy instrument on the Mars Science
1073 Laboratory rover, Spectrochimica Acta Part B, 82, 1–27.

1074

1075

1076

1077

1078

1079

1080

1081

1082

1083

1084

1085

1086

1087

1088

1089

Tables

1090 **Table 1.** VNIR determined mineralogy of all of the bulk rock samples in order of increasing
 1091 alteration determined by visual analysis (amount of red material on surface) and overall
 1092 continuum shape; underlined entries are subset used for further study. Note that all samples
 1093 have 1.9-um vibrational absorptions, so these are not listed.

Sample	Description	Overall continuum	Ferric absorptions (μm)	Vibrational Absorptions (μm)	VNIR-determined mineralogy
<u>SanC-J</u>	large dark grey basalt	flat, constant slope	-	small 1.41; small, broad 2.21; small 2.31	hydrous Si + Fe/Mg clay
SanC-K	large mottled grey/light grey basalt	flat, constant slope	-	small 1.41; broad 2.21	hydrous Si
SanC-F	small grey basalt, white coating	downward slope	-	1.50; doublet at 1.95 and 2.04; 2.21	gypsum coating
<u>SanC-C</u>	large dark brown/rust basalt	curved, concave down	0.5, 0.53, pos. UV-Vis slope, 0.89-0.99	1.41; sharp and broad 2.21	hydrous Si + Al-smectite + Fe(III)-ox.
<u>SanC-B</u>	massive grey/brown basalt	downward slope	0.5, pos. UV-Vis slope, 0.97	sharp 1.42, broad 2.21, 2.29-2.32	hydrous Si + Mg clay + Fe(III) oxide
SanC-I	large grey/rust colored basalt	downward slope	Sharp 0.53 band	1.41; 2.21 bands	Al-smectite + Fe(III) oxide
<u>SanC-A</u>	large basaltic rock, rust colored	curved, concave down	0.5, 0.53, pos. UV-Vis slope, 0.91	sharp 1.41 and 2.21 bands	Al-smectite + Fe(III) oxide

1094 **Table 2.** Band depth calculations and corresponding wavelength for all samples in order of
 1095 increasing alteration determined by visual analysis and overall continuum shape; underlined
 1096 entries are subset used for further study. The 1.9 μm band depth is an indicator of water
 1097 content, and band depths at 2.2 and 2.3 μm indicate Al-OH and Fe,Mg-OH content [e.g., *Milliken*
 1098 et al., 2005].

Sample	<u>SanC-J</u>	SanC-K	SanC-F	<u>SanC-C</u>	<u>SanC-B</u>	SanC-I	<u>SanC-A</u>
Avg wavelength	1.915	1.912	1.914	1.918	1.9132	1.914	1.917
Avg BD1900	0.072	0.113	0.101	0.068	0.128	0.166	0.155
Avg wavelength	n/a	n/a	n/a	0.529	0.526	0.526	0.532
Avg BD530	n/a	n/a	n/a	0.127	0.096	0.169	0.273
Avg wavelength	2.299	2.312	2.316	2.315	2.312	2.309	2.312
Avg BD2300	0.029	0.005	0.003	0.003	0.163	0.002	0.005
Avg wavelength	2.208	2.214	2.214	2.207	2.207	2.206	2.204
Avg BD2200	0.0285	0.039	0.024	0.043	0.020	0.070	0.099

1099

1100

1101

1102

1103 **Table 3.** Bulk chemical analysis (weight percentages) for all samples in order of increasing
1104 alteration; samples selected for further analysis are underlined.

Oxides	<u>SanC-A</u>	<u>SanC-B</u>	<u>SanC-C</u>	SanC-F	SanC-I	<u>SanC-J</u>	SanC-K
SiO ₂	44.0	43.6	44.8	45.3	44.1	45.0	45.5
TiO ₂	2.79	2.67	2.73	2.72	2.68	2.66	2.70
Al ₂ O ₃	15.0	14.7	14.6	14.8	14.7	15.1	14.6
Cr ₂ O ₃	0.00	0.00	0.00	0.00	0.00	0.00	0.00
Fe ₂ O ₃	13.5	12.5	13.4	13.1	13.1	13.3	12.9
MnO	0.20	0.19	0.20	0.20	0.20	0.20	0.20
MgO	8.03	7.80	9.04	8.35	7.79	7.40	8.08
CaO	7.90	7.74	7.66	7.64	7.73	7.38	7.58
Na ₂ O	3.34	4.86	3.92	5.27	4.30	4.62	5.27
K ₂ O	2.27	1.16	2.55	1.48	1.28	2.84	1.28
P ₂ O ₅	0.75	0.73	0.77	0.79	0.85	0.86	0.85
TOTAL	97.0	95.2	98.9	98.8	95.8	98.4	98.1
Loss	3.0	4.8	1.1	1.2	4.2	1.6	1.9
CaO+Na ₂ O+K ₂ O	55.25	56.21	56.4	58.16	56.16	56.97	58.32
Na ₂ O + K ₂ O	5.61	6.02	6.47	6.75	5.58	7.46	6.55

1105

1106 *All Fe is reported as Fe₂O_{3(T)}

1107

1108

1109

1110

1111

1112

1113 **Table 4.** Normative mineralogy calculated using the CIPW method from bulk chemical analysis.
 1114 Modal mineralogy (italicized in parentheses) calculated by combining averages of measured
 1115 mineral compositions from microprobe spot analyses and phase proportions from Rietveld
 1116 refinement of bulk compositional XRD data.

Mineral	<u>SanC-A</u>	<u>SanC-B</u>	<u>SanC-C</u>	SanC-F	SanC-I	<u>SanC-J</u>	SanC-K
Feldspar	38.92 <i>(32)</i>	36.99 <i>(24)</i>	29.01 <i>(29)</i>	33.29	41.92	26.29 <i>(31)</i>	36.31
Orthoclase	14.25 <i>(0)</i>	7.50 <i>(8.5)</i>	15.55 <i>(3.5)</i>	9.10	8.22	17.38 <i>(0)</i>	8.05
Nepheline	5.24 <i>(12)</i>	11.69 <i>(12)</i>	10.28 <i>(12)</i>	12.85	7.06	13.53 <i>(23)</i>	11.47
Leucite	0.00 <i>(10)</i>	0.00 <i>(10)</i>	0.00 <i>(7)</i>	0.00	0.00	0.00 <i>(0)</i>	0.00
Hi-Ca Pyroxene	10.50 <i>(19)</i>	16.19 <i>(18)</i>	14.81 <i>(22)</i>	16.43	13.46	15.46 <i>(21)</i>	16.24
Olivine	17.17 <i>(12)</i>	14.61 <i>(10)</i>	17.06 <i>(11)</i>	15.11	15.77	14.00 <i>(13)</i>	14.72
Ilmenite	5.47 <i>(0)</i>	5.32 <i>(1.5)</i>	5.22 <i>(0)</i>	5.22	5.30	5.11 <i>(0)</i>	5.22
Magnetite	6.08 <i>(7)</i>	5.70 <i>(7.5)</i>	5.86 <i>(10)</i>	5.76	5.92	5.84 <i>(13)</i>	5.70
Hematite	0.00 <i>(4)</i>	0.00 <i>(5)</i>	0.00 <i>(5)</i>	0.00	0.00	0.00 <i>(2)</i>	0.00
Total	99.55	99.82	99.73	99.76	99.82	99.77	99.81

1 **Revision 2**

2 **Figure Captions**

3 Figure 1. TAS diagram showing the composition of the 7 San Carlos rocks with varying
4 degrees of aqueous alteration examined in this study. All samples plot in the basanite
5 field with SiO₂ weight percentages between 44 and 44.5 % and total alkali percentages
6 between 5.6 and 7.4 %. Dark gray circles show the composition of Jake Matijevic,
7 Bathlet Inlet, Rocknest, and Et-Then from APXS analyses at Gale crater on Mars (Stolper
8 et al., 2013). Smaller light gray circles show the compositions of all ChemCam analyses
9 at Gale crater (up to August 9, 015). Plotted ChemCam analyses were not filtered for
10 igneous samples, and the distribution of points exhibits the compositional diversity of
11 igneous float rocks and the igneous protoliths sampled by sedimentary rocks.

12
13 Figure 2. (a) Location of the San Carlos Peridot Mesa in San Carlos, AZ and an outcrop
14 of basalt with olivine xenoliths. (b) basalts ordered from least to most altered based on
15 visual appearance. Sample J; least altered basalt with bright green olivine xenoliths.
16 Sample K; relatively pristine basalt. Sample F; relatively pristine basalt with gypsum
17 coating. Sample B; intermediately altered basalt with friable olivine xenoliths (f) Sample
18 C; intermediately altered basalt with red-brown olivine xenoliths. Sample I; highly
19 altered red-brown basalt with friable olivine. Sample A; most altered red-brown basalt
20 with reddish olivine xenoliths.

21
22 Figure 3. (a) Average spectra for all 7 samples; features at 0.53, 1.0, 1.4, 1.9, 2.2, and 2.3
23 μm were used to identify primary and secondary mineralogy in each sample. (b)
24 Continuum removed endmember spectra of the 4 endmembers-J,B,C, and A- between
25 0.35 and 1.35 μm . This region was used to identify ferric iron features near 0.5 μm , as
26 well as ferrous iron features near 1.0 μm . (c) Reference spectra of iron oxides from the
27 USGS Spectral Library [Clark et al., 2007a] between 0.5 and 1.3 μm . (d) Continuum
28 removed endmember spectra of the 4 endmembers - J, B, C, and A - between 2.0 and 2.5
29 μm . This region was used to identify metal-OH absorption features that are indicative of
30 phyllosilicates; absorption bands at 2.2 and 2.3 μm are indicative of Si-OH or Al-OH and
31 Fe-OH of Mg-OH, respectively. (e) Reference spectra of phyllosilicates from the USGS
32 Spectral Library [Clark et al., 2007a] between 2.0 and 2.5 μm . (f) Spectral variability in
33 Sample J; key absorptions are at 1.9, 2.2, and 2.29-2.30 μm . (g) Spectral variability in
34 Sample B; key absorptions are at 1.9 and 2.31 μm . (h) Spectral variability in Sample C;
35 key absorptions are at 1.9 and 2.2 μm . (i) Spectral variability in Sample A; strong
36 absorptions are at 1.9 and 2.2 μm .

37
38 Figure 4. Examination of the correlation of absorption band depths for (a) 0.53 μm vs 1.9
39 μm , (b) 2.2 μm vs. 1.9 μm , (c) 2.3 μm vs. 1.9 μm , (d) 0.53 μm vs. 2.2 μm and (e) 2.3 μm
40 vs. 2.2 μm . Band depths tracking hydration (BD1900), iron oxidation (BD530), and Si-
41 OH/Al-OH content (BD2200) are directly correlated; no trend is apparent for band depths
42 tracking Fe-OH/Mg-OH content.

43
44 Figure 5. Back-scattered electron images of alteration textures. (a) Unaltered primary
45 minerals in SanC-J; lath-shaped grains are feldspar, dark interstitial phases are nepheline.

46 (b) Wormy olivine textures from replacement by hematite veins in SanC-B; mottled,
47 plagioclase dissolution texture in upper left and lower right. (c) Unaltered minerals on
48 SanC-C near the sample edge. (d) Low magnification image of SanC-A edge; white
49 square is (e). (e) Olivine altered to contain hematite veins, mottled titanomagnetite, and
50 mottled feldspar laths. (f) Different edge in SanC-A showing similar textures to (d). (g)
51 Area around altered olivine rim in SanC-B. (h) BSE image in SanC-A interior showing
52 an overall texture similar to that in SanC-C (b).
53
54

55 Figure 6. (a) Mg# (Mg over the sum of MgO, MnO, and FeO) vs Na,K,Al, Ca, and Ti
56 oxides for olivine (in weight percent) calculated on the basis of four oxygen atoms from
57 microprobe analyses. As described in the text, the observed compositional variation is
58 partly primary and partly an effect of alteration. (b)-(d) Weight percent oxide plots from
59 microprobe analyses of olivine grains (hem = hematite). (b) MgO vs. SiO₂ wt.%;
60 deviations from the Fo-Fa line represent alteration, primarily in the formation of veinlets
61 of hematite. (c) FeO vs. SiO₂ wt.%; variation along the Fo-Fa line indicates changes in
62 composition from olivine grain Mg-rich cores to more Fe-rich rims, a primary
63 compositional variation. (d) Primary variance in MgO and FeO from magnesian cores to
64 ferroan rims; deviations from the Fo-Fa line and FeO enrichment indicate the occurrence
65 of hematite veining in more Fe-rich rims.
66

67 Figure 7. Composition of pyroxene (in mole percent) calculated on the basis of six
68 oxygen atoms, as determined by electron microprobe analyses of thin sections; most
69 pyroxenes plot in the augite and pigeonite fields.
70

71 Figure 8. Weight percent oxide plots from microprobe analyses of opaques (ulvosp=
72 ulvöspinel TiFe²⁺₂O₄; mag=magnetite Fe²⁺Fe³⁺₂O₄; hem=hematite Fe³⁺₂O₃, ilm=ilmenite
73 Fe²⁺TiO₃) calculated on the basis of four oxygen atoms (a) Composition of Fe-Ti oxides
74 from electron microprobe analyses (b) most of the oxide compositions fall along a join
75 between ulvöspinel and Ti-rich magnetite (c) more altered samples also trend towards
76 hematite as titanomagnetite is oxidized.
77

78 Figure 9. (a) Composition of feldspars (in mole percent) calculated on the basis of eight
79 oxygen atoms, as determined by electron microprobe analyses; most feldspars plot in the
80 plagioclase field with the exception of a few analyses of alkali feldspar rims in SanC-B
81 and C.
82

83 Figure 10. (a) Composition of potential clay minerals (in mole percent) calculated on the
84 basis of eleven oxygen atoms, as determined by electron microprobe analyses; most clay-
85 like minerals in SanC-A plot near montmorillonite (Mont), consistent with spectral data.
86 Clay-like compositions in SanC-B plot along the Fe-Mg axis, indicating the presence of
87 more Fe,Mg rich phyllosilicates. The single SanC-B analysis near the Al-vertex was
88 taken from altered material between plagioclase laths; most phyllosilicate-like
89 compositions for B were found near altered olivine grains, and few phyllosilicates were
90 found near plagioclase laths. No clays were found with microprobe in SanC-J or SanC-C.
91 Labeled points on ternary are shown in BSE images for (b) SanC-A and (c) SanC-B.
92

93 Figure 11. (a) XRD spectra offset along the y-axis arranged from most altered (A) to least
94 altered (J) showing sharp peaks from primary mineralogy, and broader features due to the
95 presence of amorphous phases. The primary hematite peak is labeled in Sample A to
96 show the change due to alteration from the Sample J to A (b) Calculated mineral
97 abundances (in weight percent) from XRD Rietveld analyses with endmember
98 compositional information determined from microprobe analyses.

99
100 Figure 12. Bulk chemical data in weight percent vs. silica for all samples; samples
101 selected for further study from spectra are shown in bold text, (a) alkalis vs. SiO_2 , (b)
102 Na_2O vs. SiO_2 , (c) CaO vs. SiO_2 , (d) $\text{Fe}_2\text{O}_{3\text{T}}$ vs. SiO_2 , (e) Al_2O_3 vs. SiO_2 , (f) MgO vs.
103 SiO_2 , (g) TiO_2 vs. SiO_2 . Trends are enrichment in Fe(III) and depletion of Si and Na due
104 to alteration. The trend in Ca may be due to primary compositional variation and/or its
105 relative enrichment as other elements are depleted (see Figure 12c). Variation in Ti and
106 Mg are due to differences in petrogenesis.

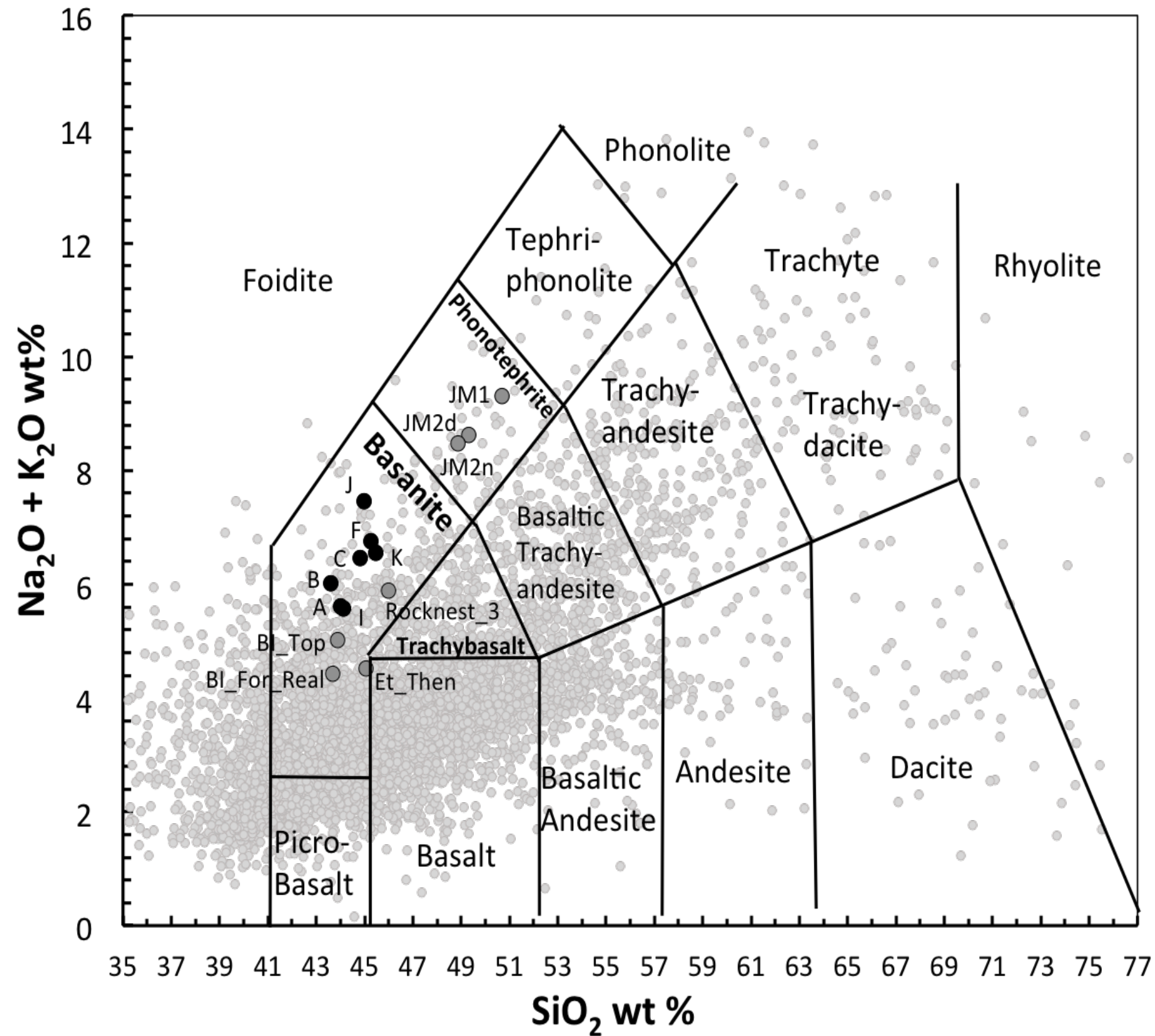
107
108 Figure 13. Loss on ignition (LOI) versus various oxides in weight percent (a) SiO_2 , (b)
109 alkalis, and (c) CaO track alteration with depletion in alkalis and silica, and slight
110 enrichment in Ca with increasing LOI, which is interpreted to represent hydration of the
111 sample upon alteration.

112
113 Figure 14. Weight percent oxides versus band depth at $1.9 \mu\text{m}$ (BD1900; tracks H_2O) for
114 all samples; bold types indicate sample subset used for further analyses (a) general
115 weathering trend of depletion in alkalis with increasing alteration (water content) due to
116 weathering of plagioclase, (b) slight trend in CaO with water content perhaps caused by
117 persistence of plagioclase and Ca-rich pyroxene as samples are weathered; no evidence of
118 Ca-salt precipitation was observed within the rock though exterior surfaces of Sample F
119 had acquired precipitated gypsum, (c) MgO , and (d) $\text{Fe}_2\text{O}_{3\text{T}}$ shows no consistent trends
120 with BD1900, possibly because of different alteration styles observed in particular
121 samples.

122
123 Figure 15. Weight percent oxide versus band depth at 0.53 microns (BD530; tracks
124 Fe(III)-oxides) for (a) alkalis vs. BD530 which shows a trend in depletion of alkalis
125 (controlled by Na) with increasing BD530, (b) Na_2O vs. BD530 which shows the trend in
126 alkali depletion is dominated by loss of Na, (c) $\text{Fe}_2\text{O}_{3\text{T}}$ vs. BD530 shows increasing
127 oxidation ferric iron content, and (d) CaO vs. BD530 shows a small enrichment in Ca.
128 SanC-B is an outlier (as in Figure 14d) for iron.

129
130 Figure 16. Ternary diagram of Al, Ca/Na/K, and Fe/Mg for bulk compositions (in mole
131 percent) of all samples (labeled with sample letters); red circles show the fields for
132 feldspars/feldspathoids, pyroxenes, and olivine. The arrow shows the general open-
133 system weathering trend for basalts after Nesbitt and Wilson, 1992. Closed symbols
134 represent primary minerals, while open symbols show altered minerals.

135
136 Figure 17. Overall weathering trends from (a) spectral and bulk chemical data, (b)
137 spectral data at longer wavelengths, (c) secondary textures and point analyses from the
138 microprobe, and (d) primary and secondary mineralogy. Arrows indicate the direction
139 from least to most altered.



San Carlos, AZ



SanC-J

Sample J

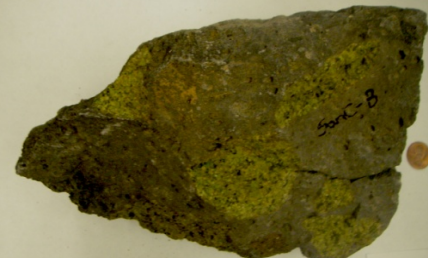


SanC-K

Sample K



Sample F



SanC-B

Sample B



SanC-C

Sample C



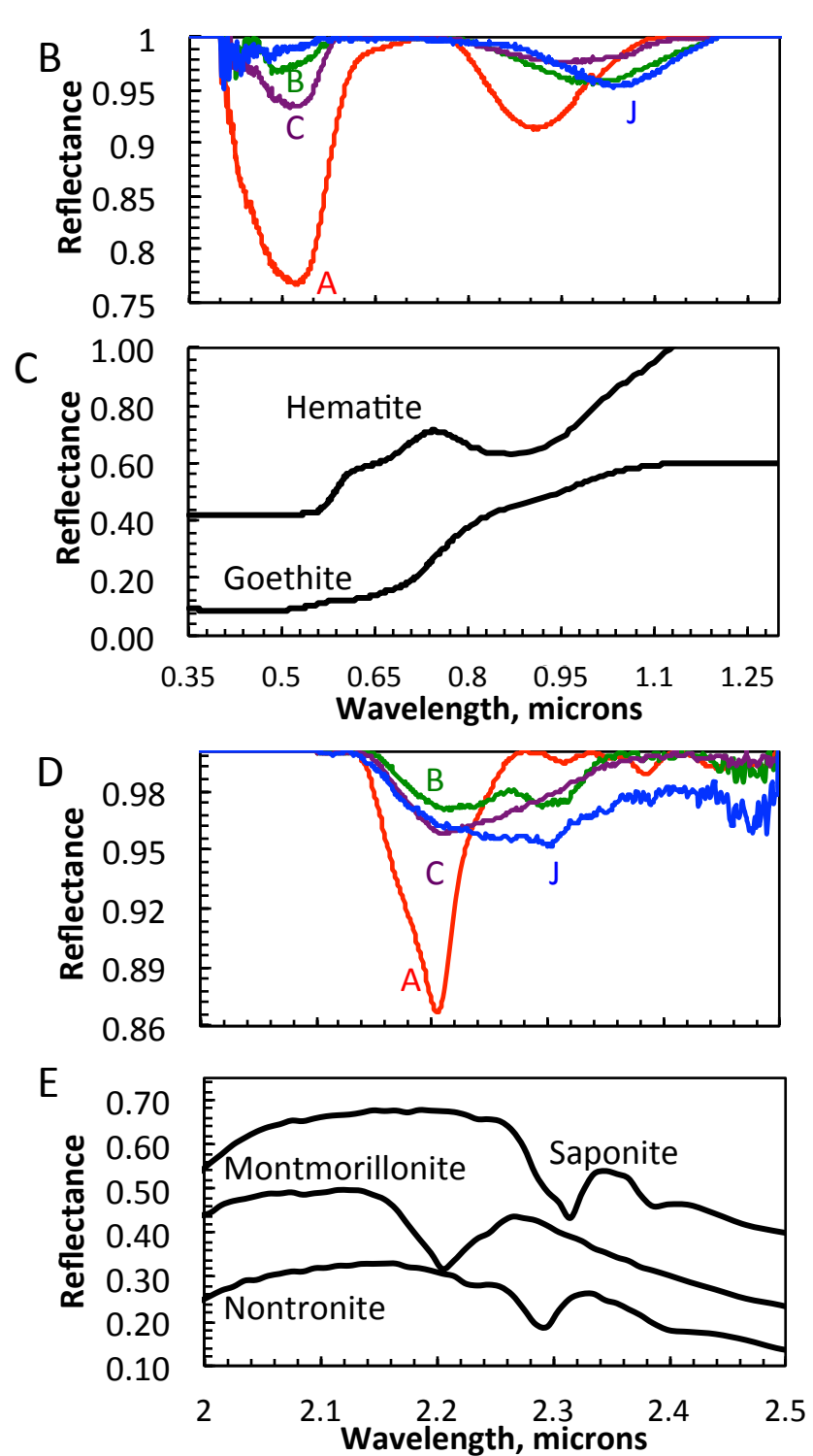
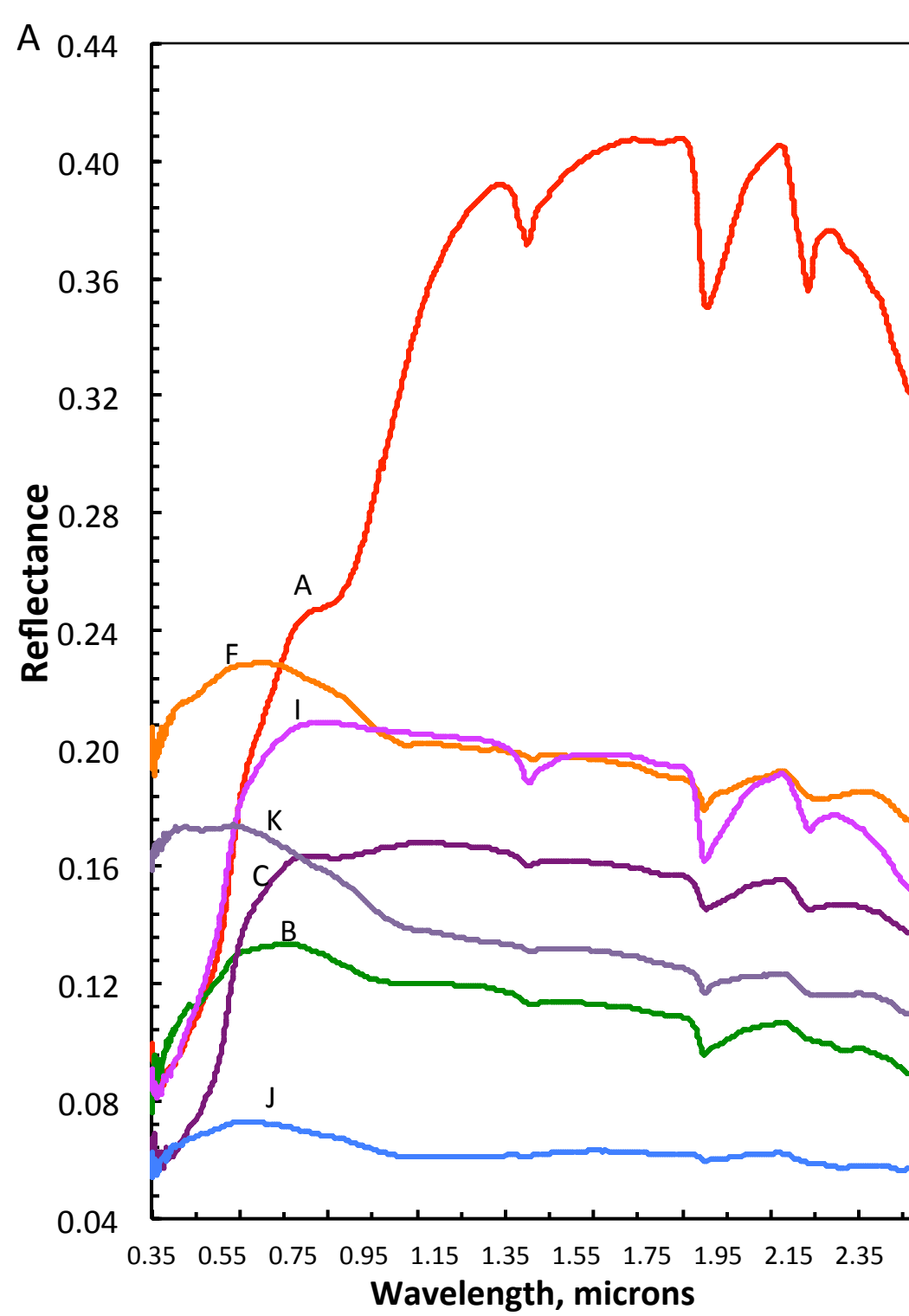
SanC-I

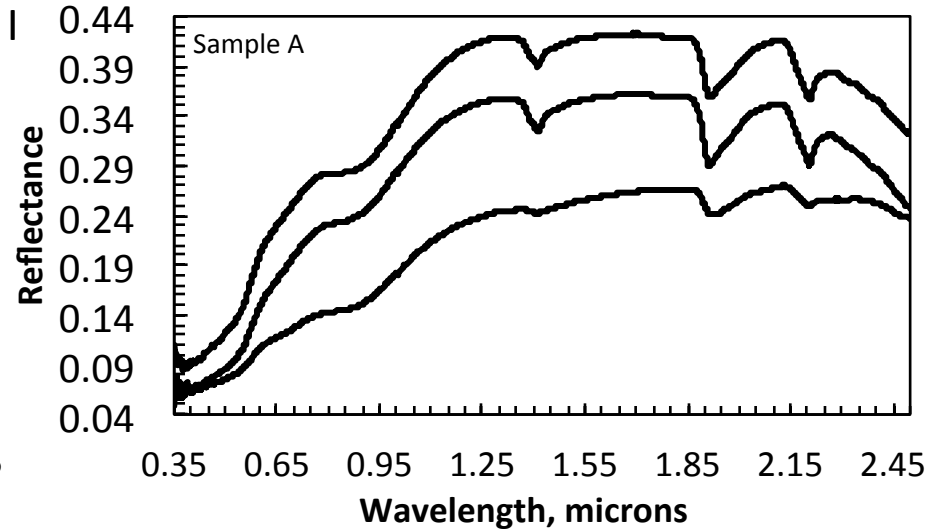
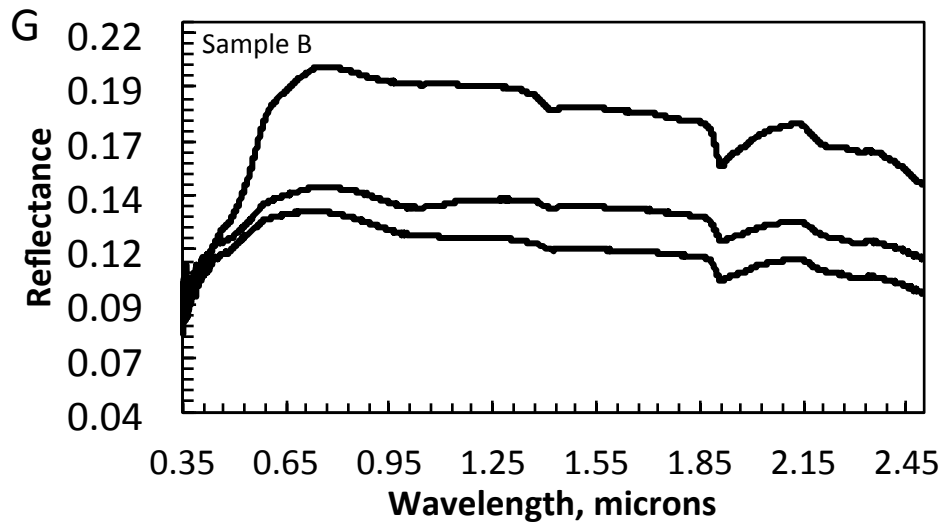
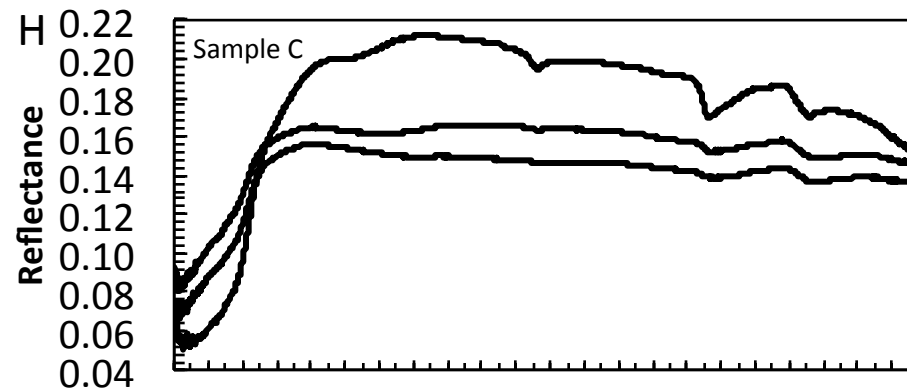
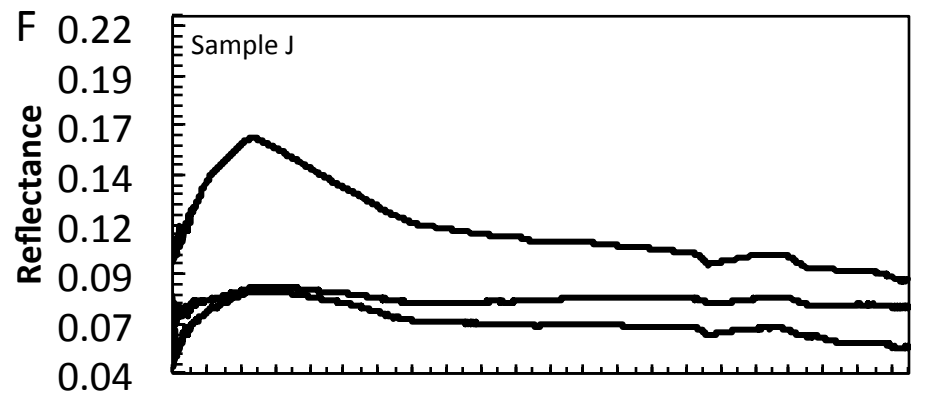
Sample I

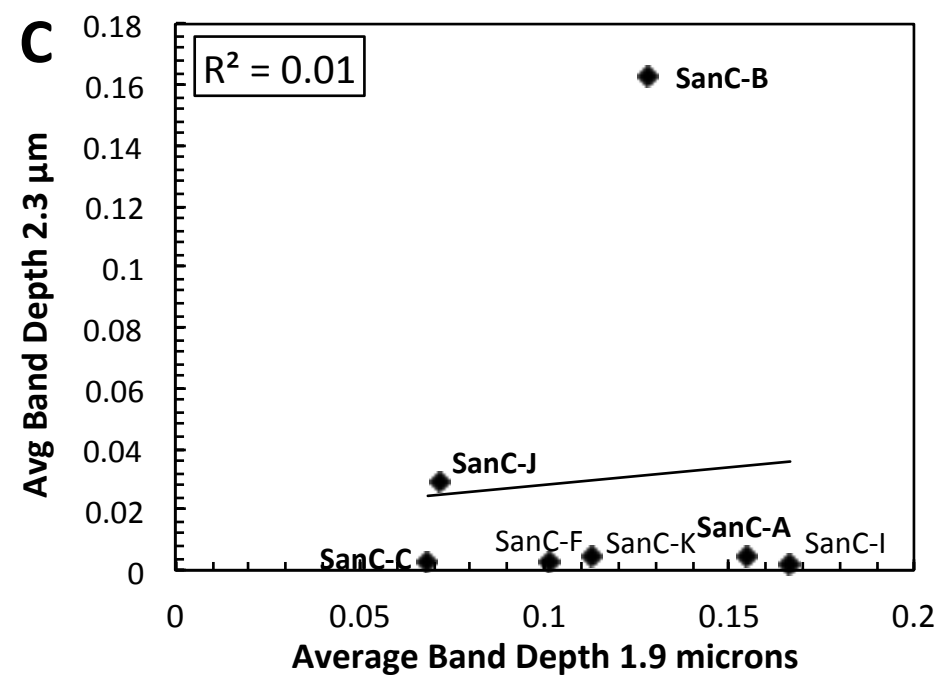
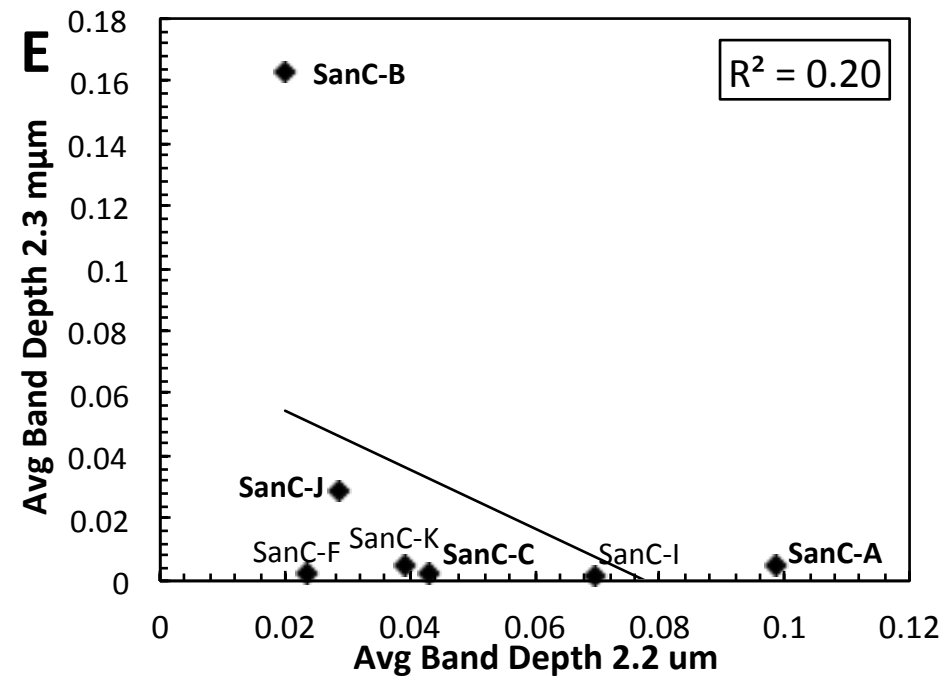
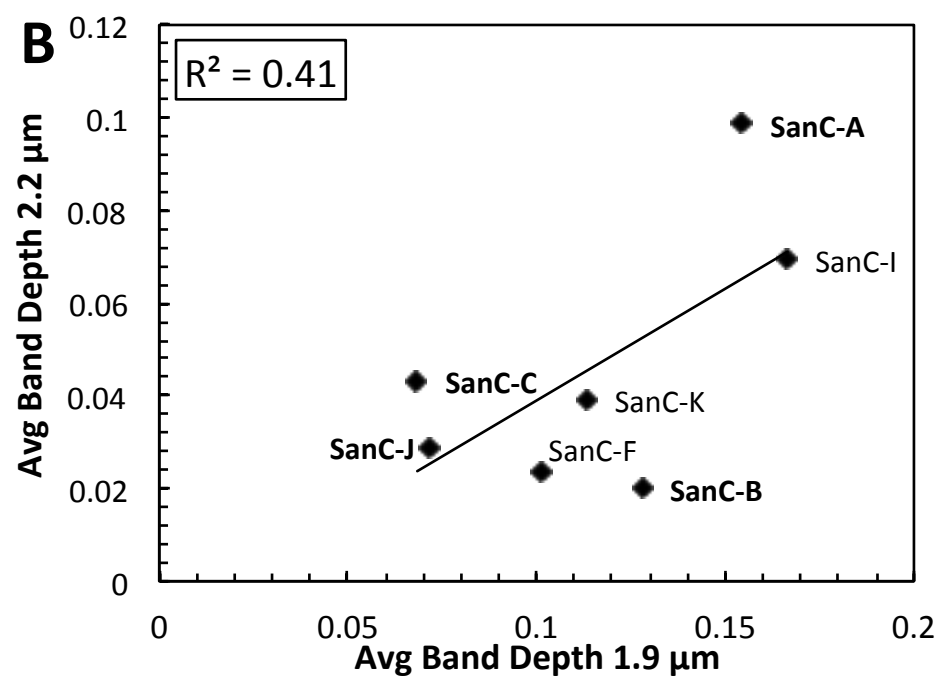
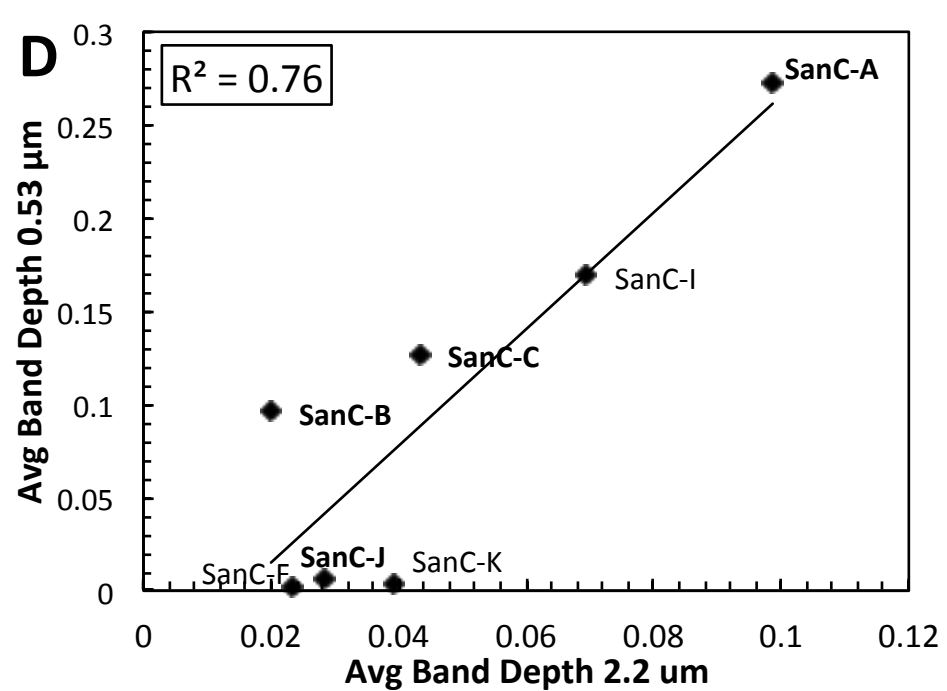
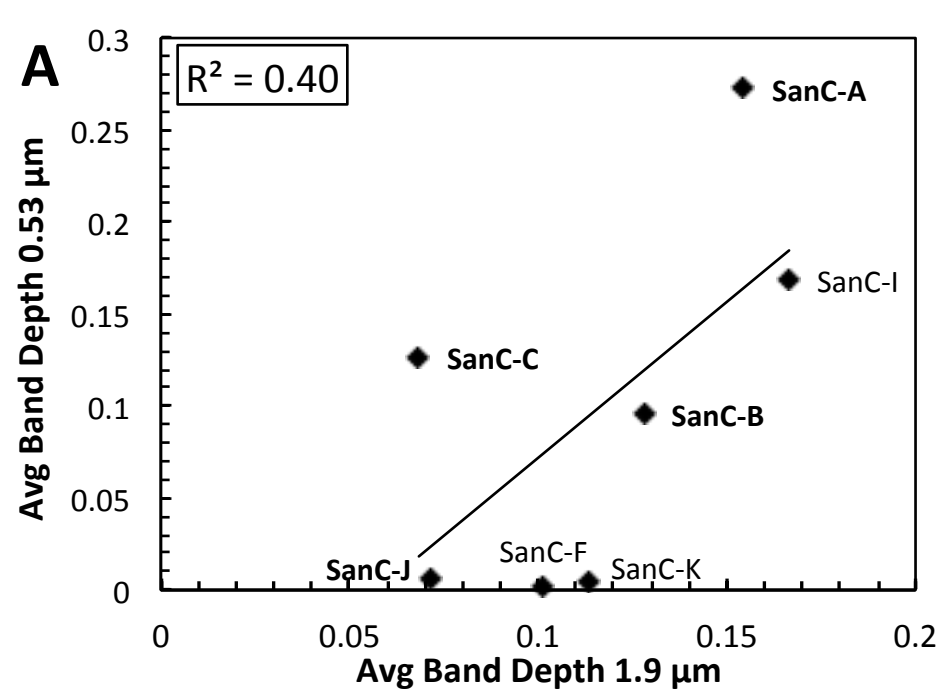


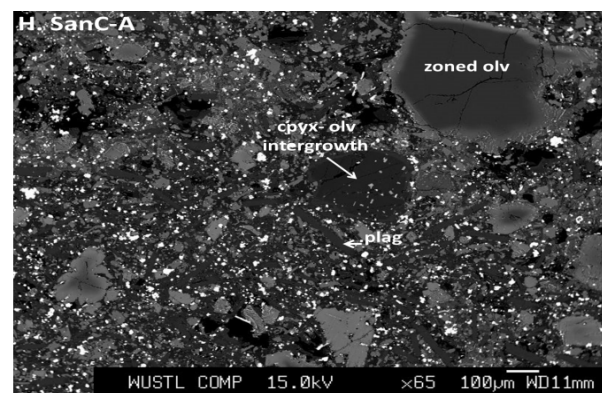
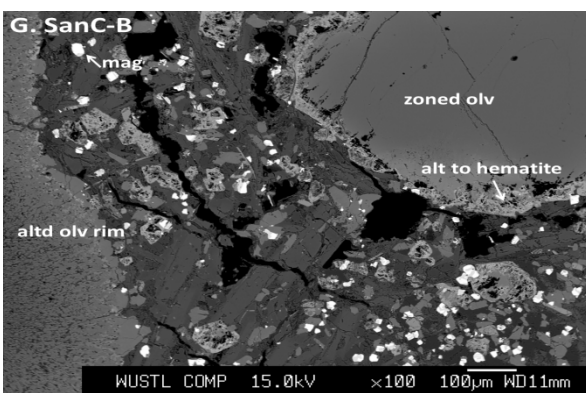
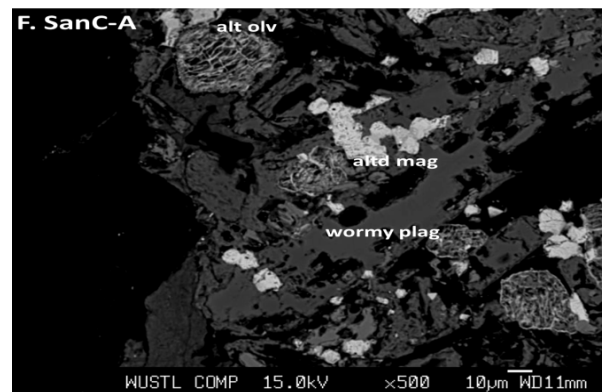
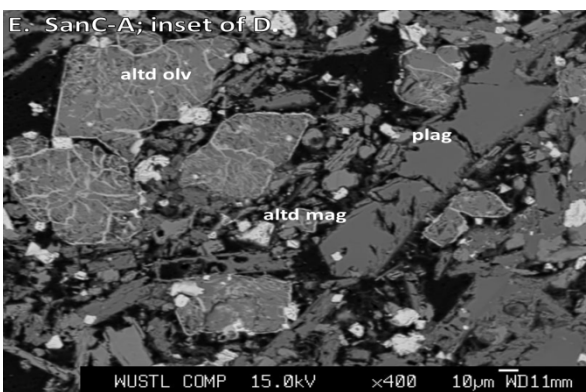
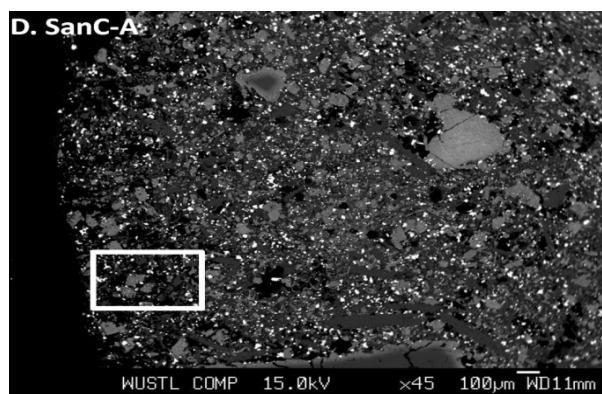
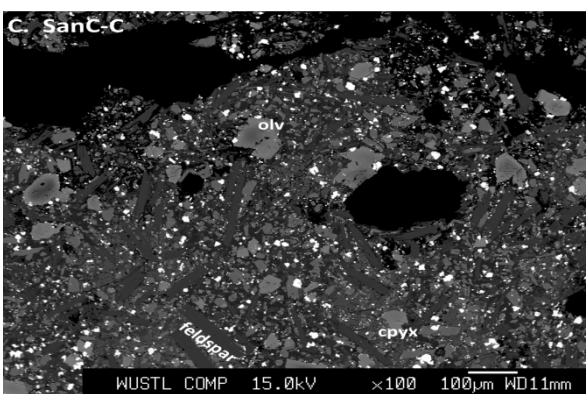
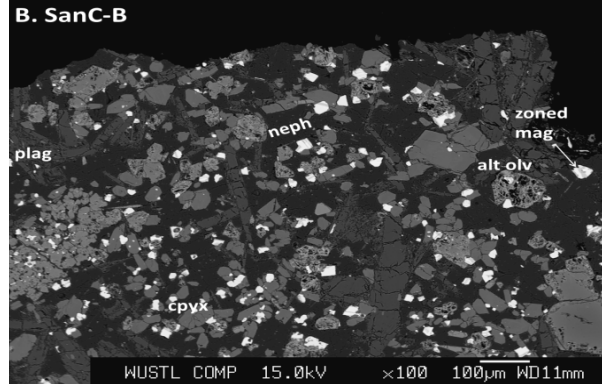
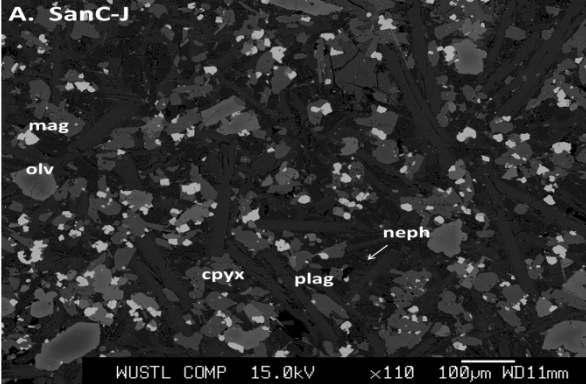
SanC-A

Sample A

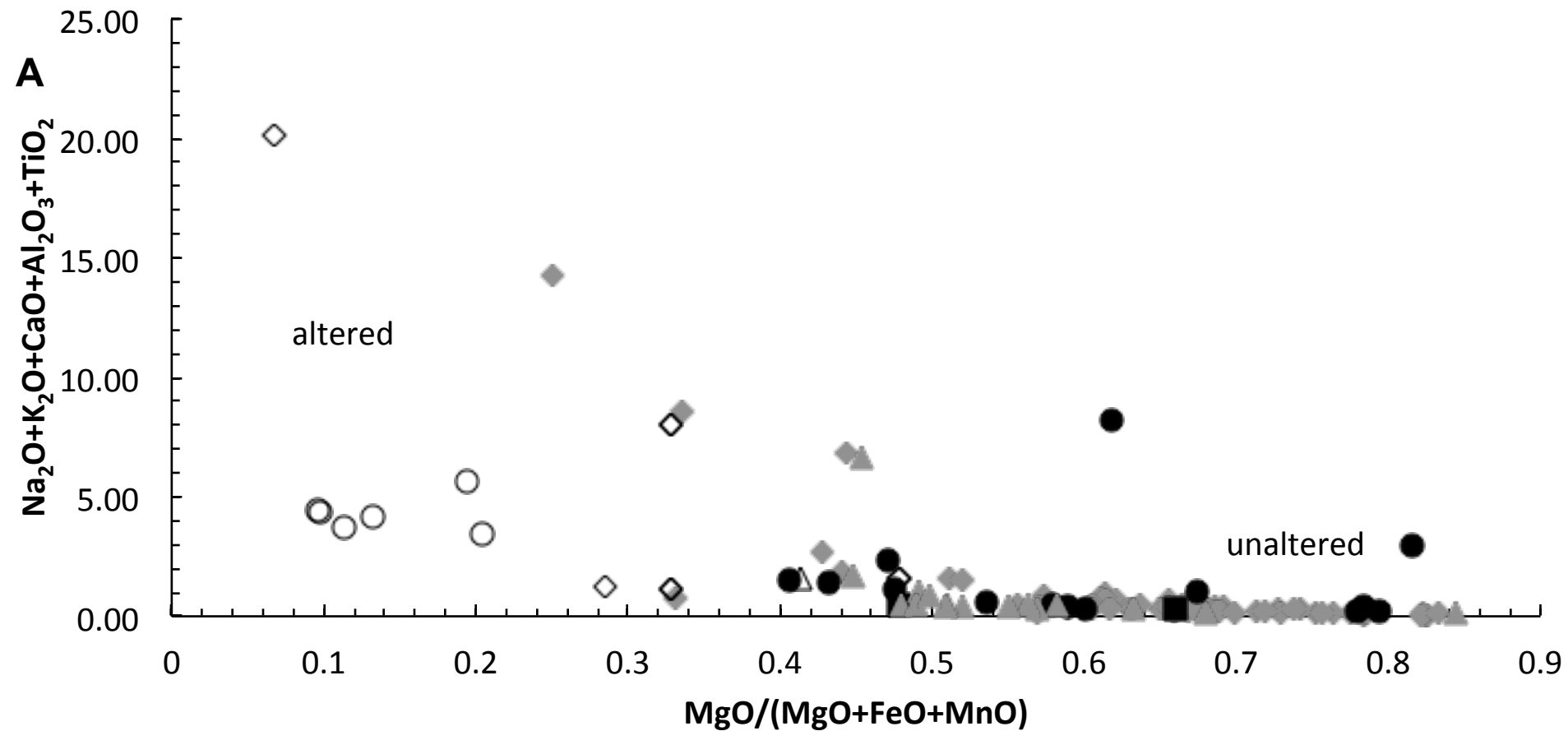


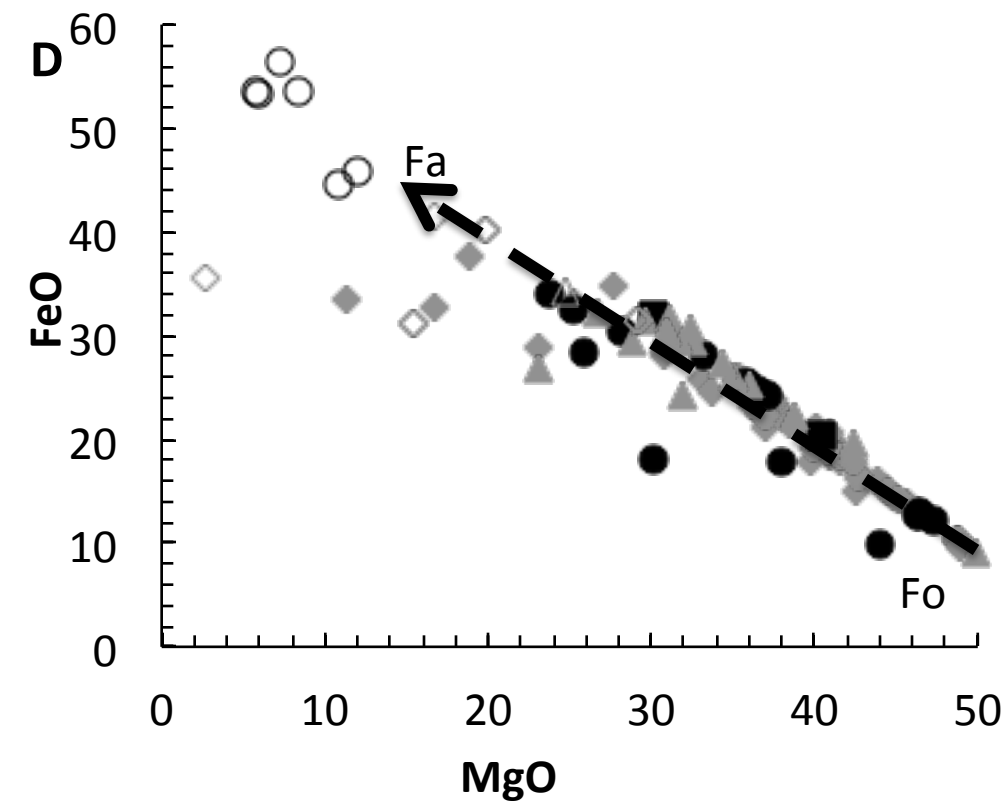
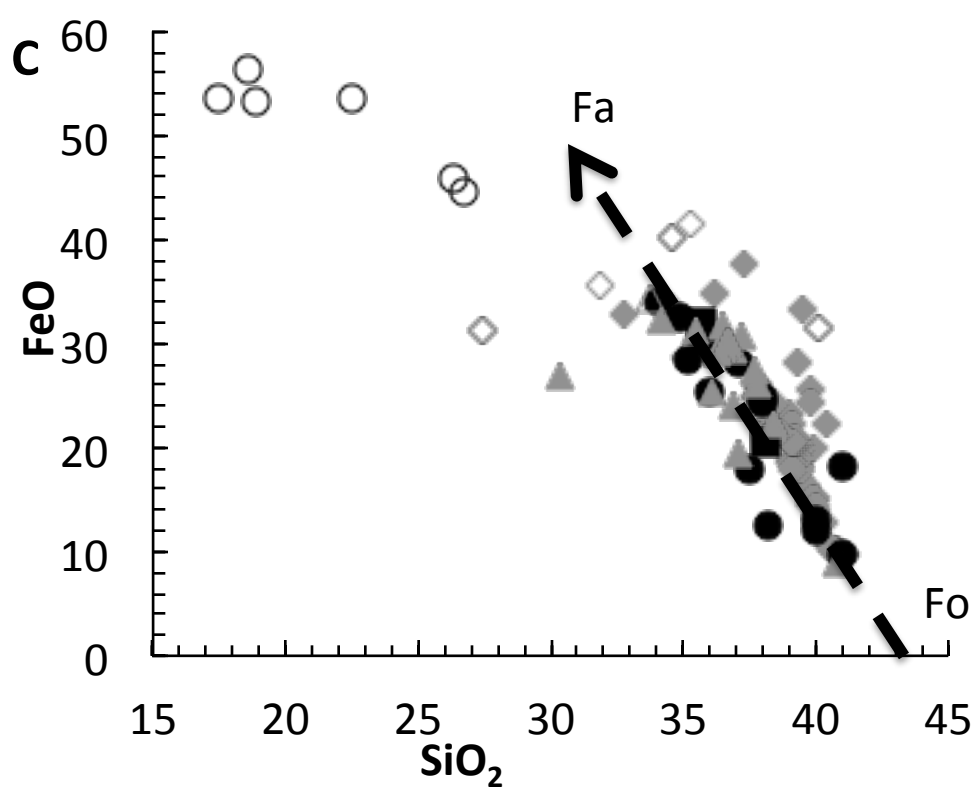
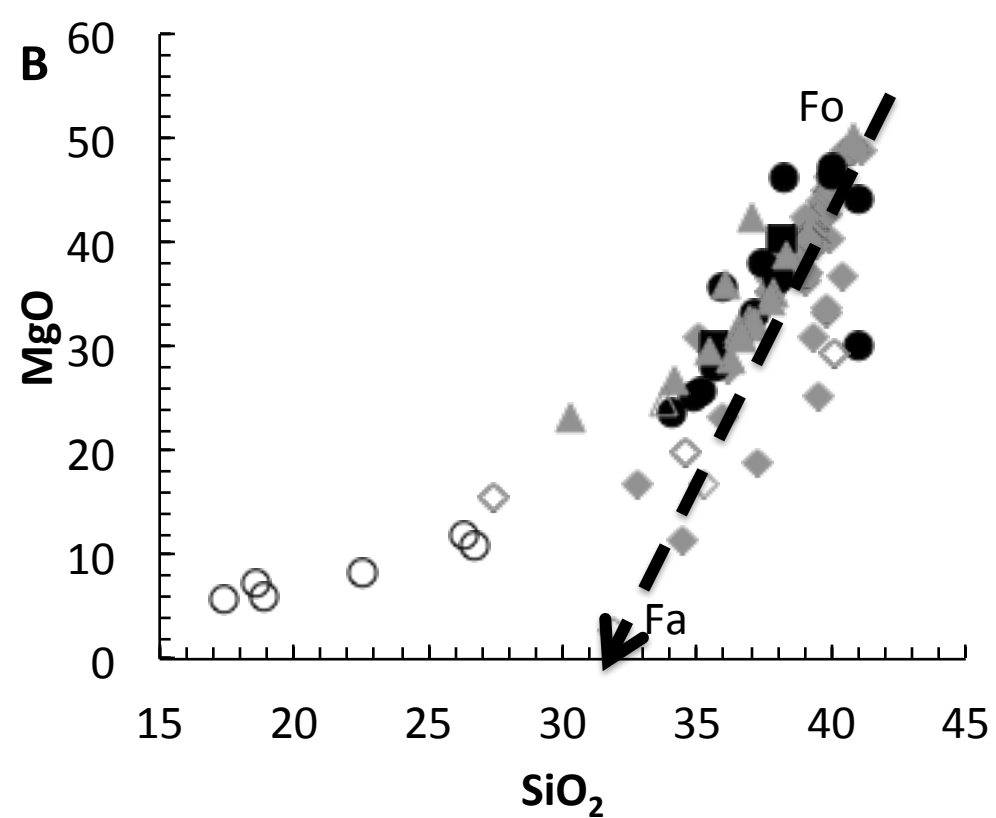




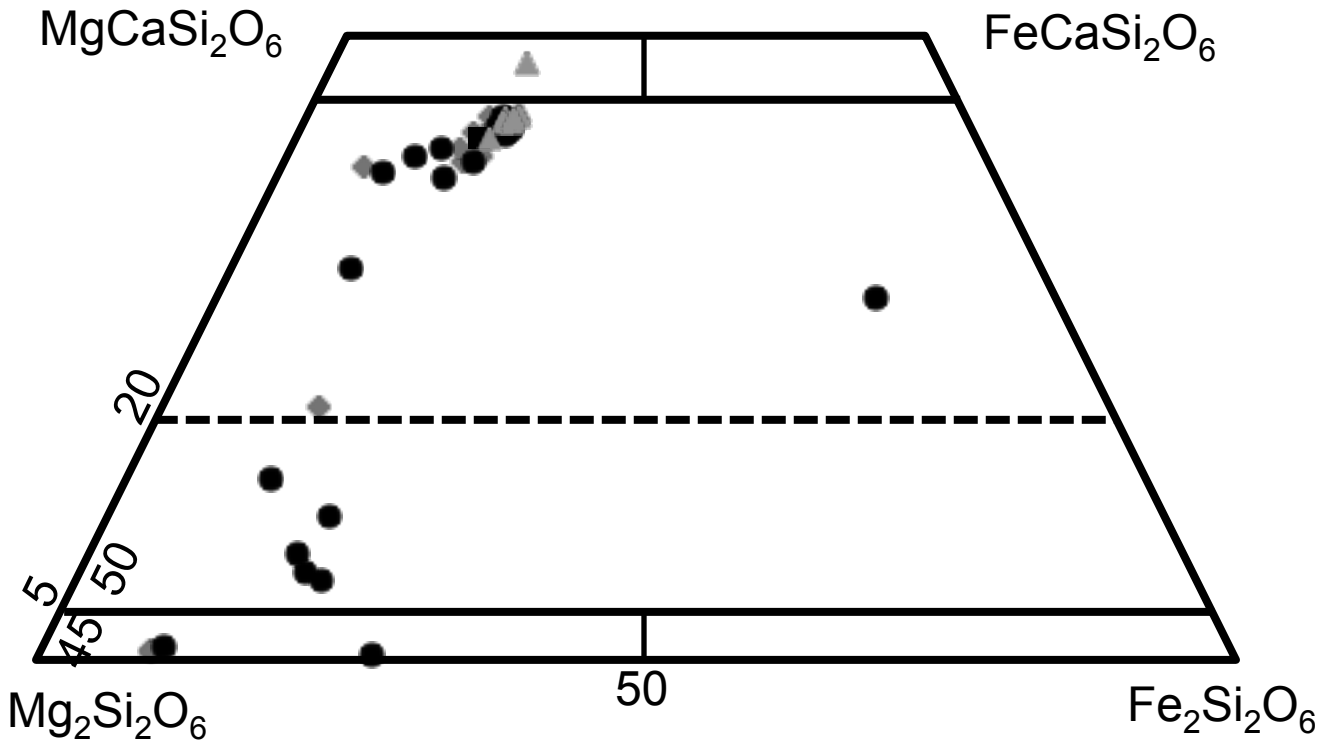


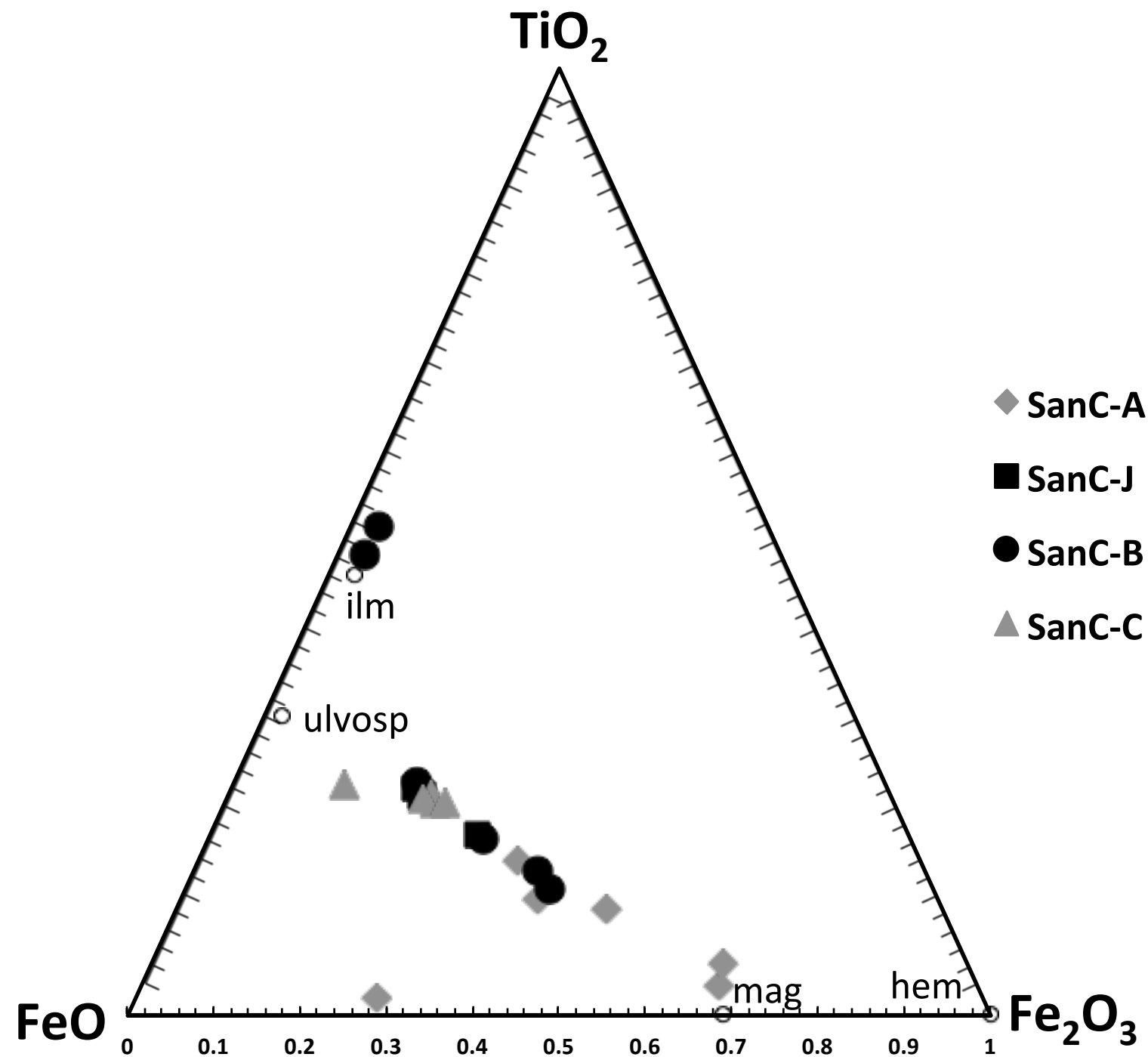
- ◆ SanC-A olv
- SanC-B olv
- ◇ SanC-A olv and hem
- △ SanC-C olv and hem
- SanC-J olv
- ▲ SanC-C olv
- SanC-B olv and hem

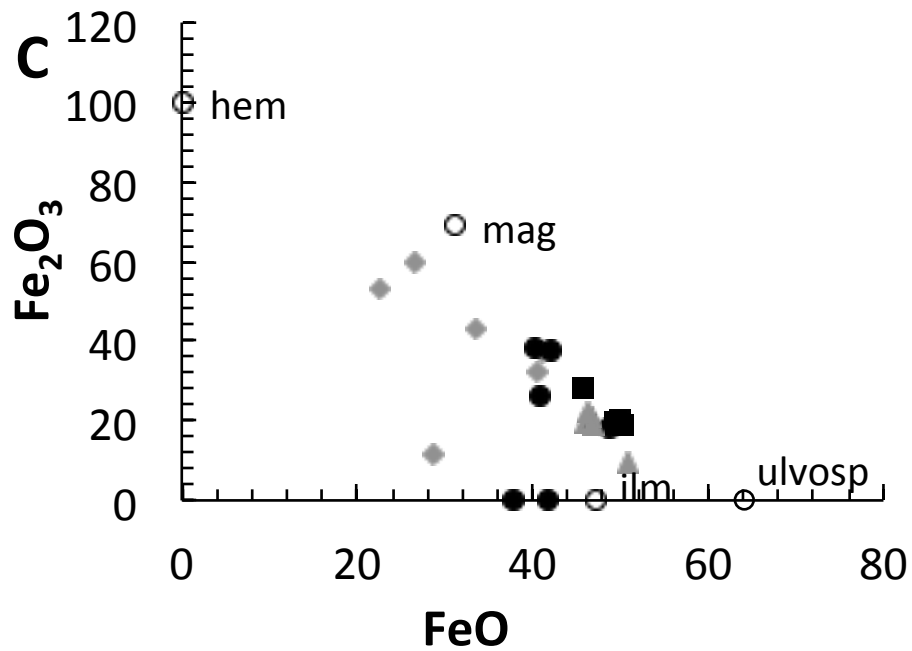
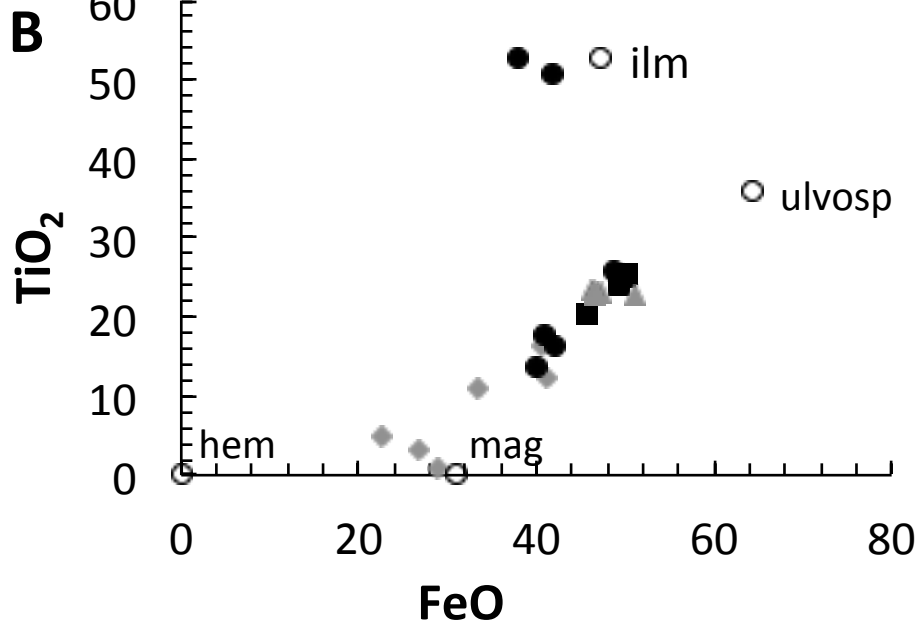


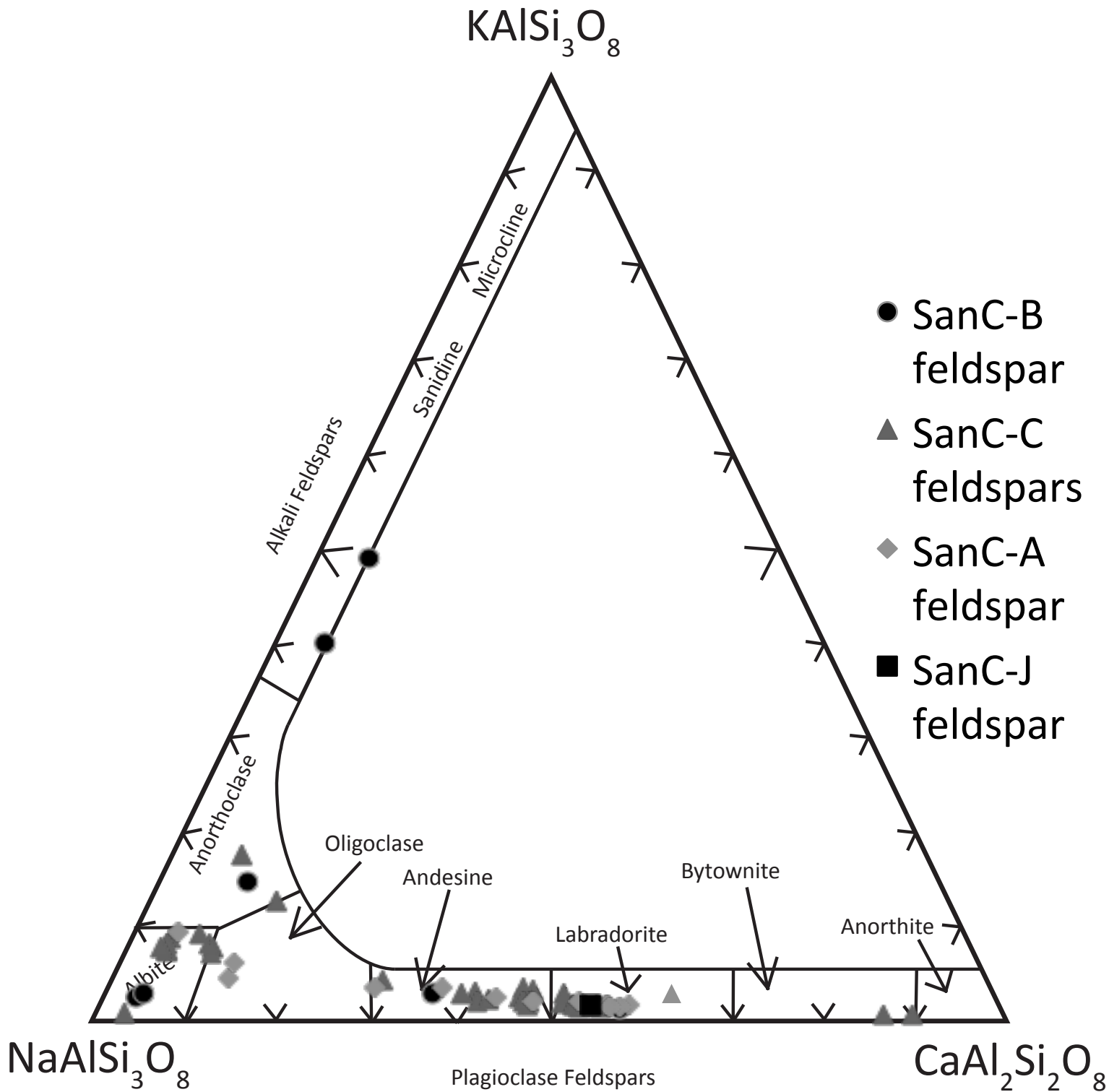


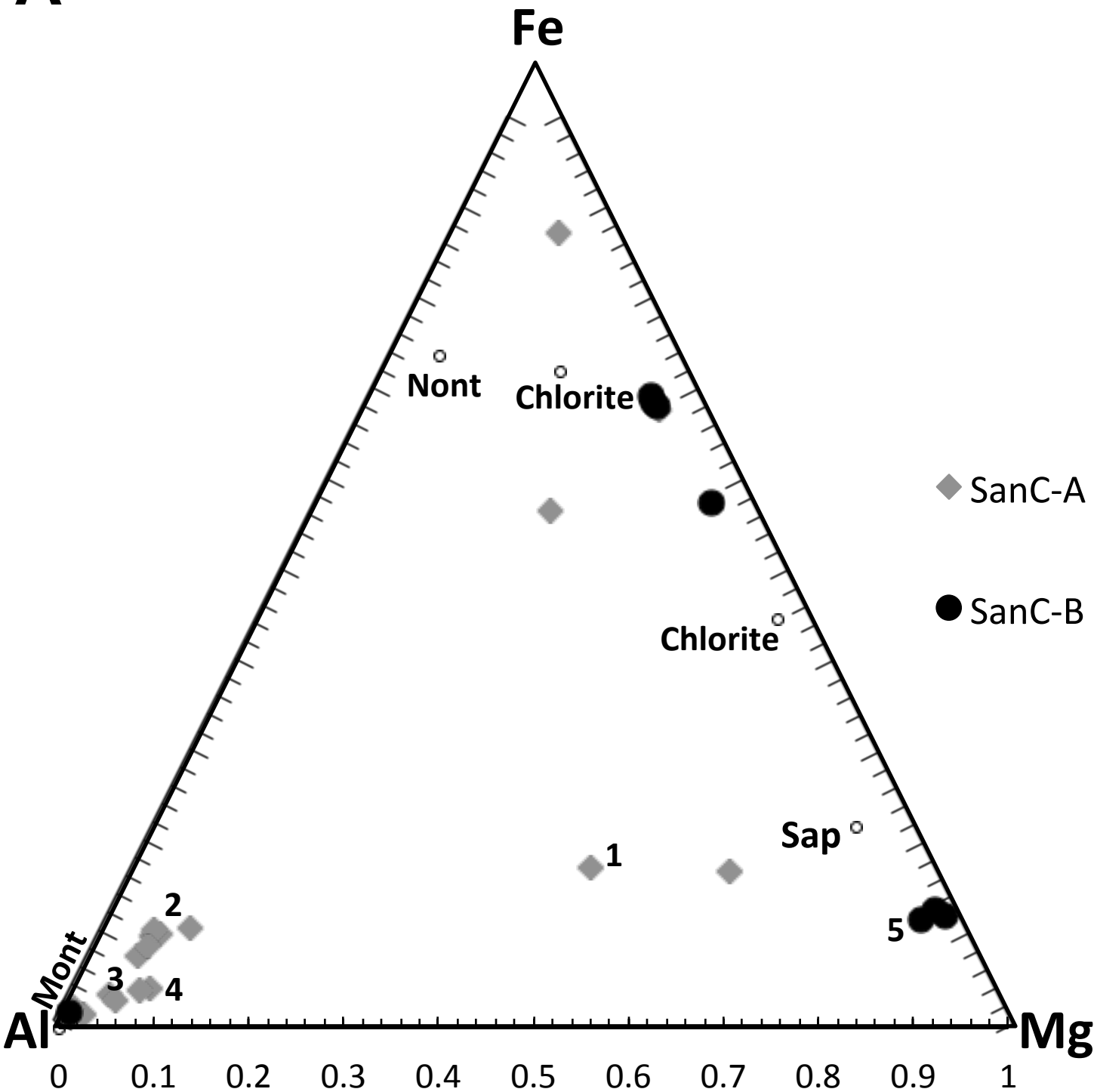
- ◆ SanC-A pyx
- SanC-J pristine pyx
- SanC-B pyx
- ▲ SanC-C pyx



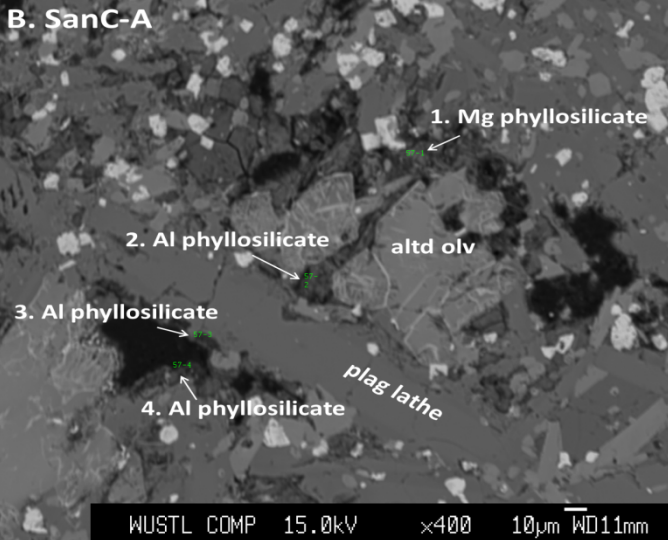
A



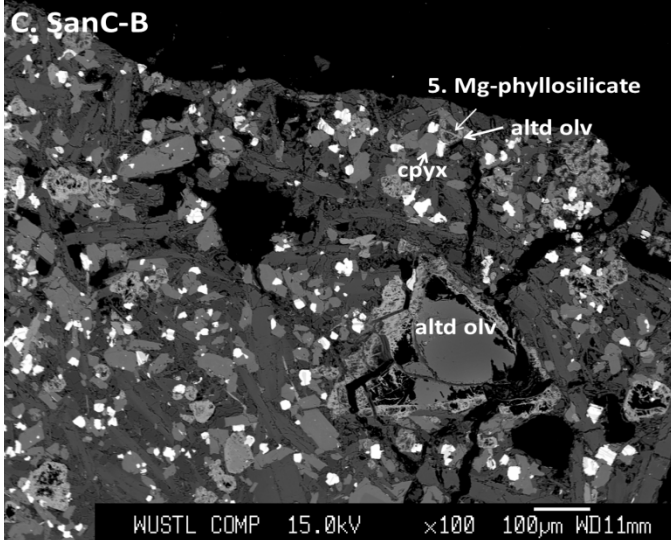


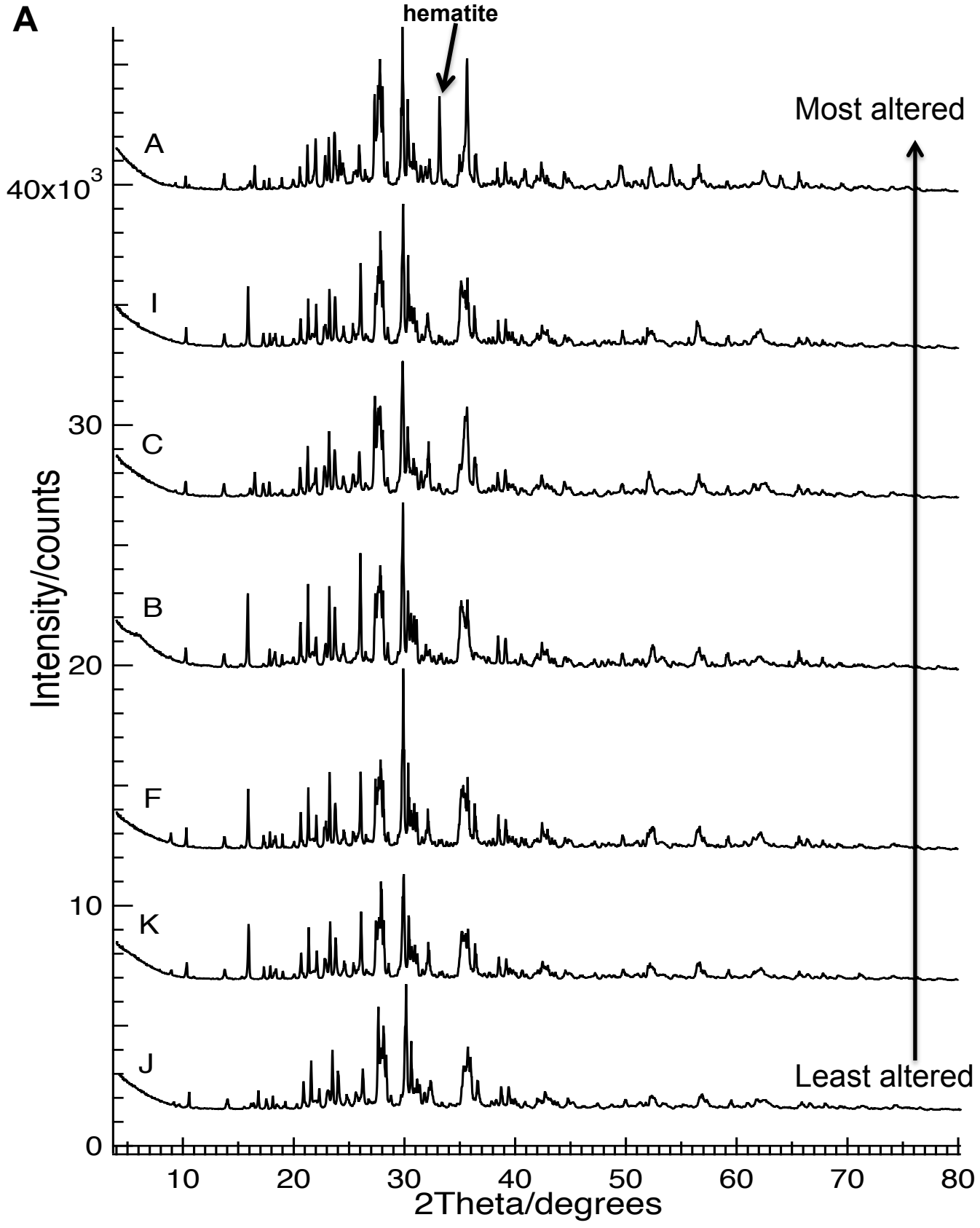
A

B. SanC-A



C. SanC-B





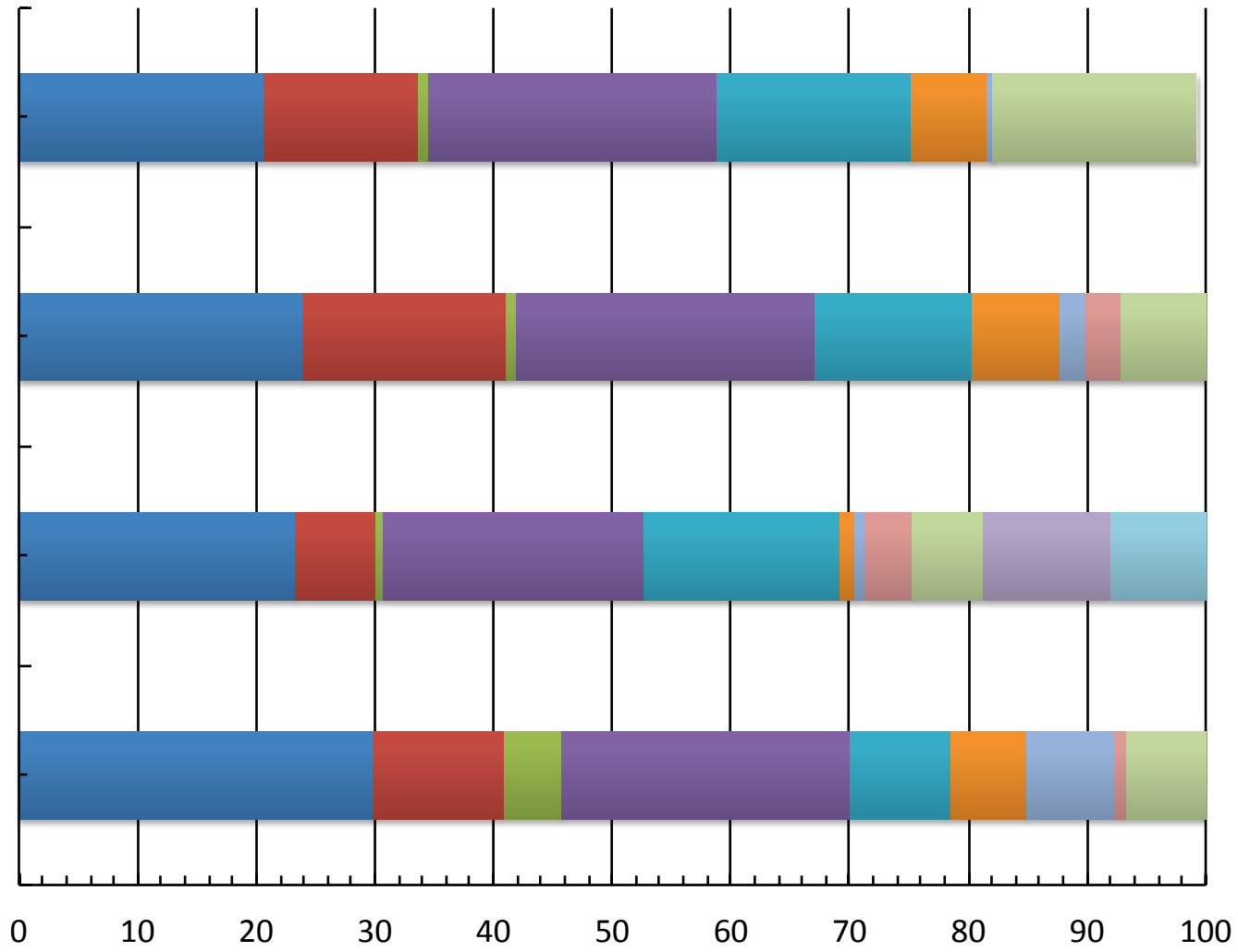
B

Sample J

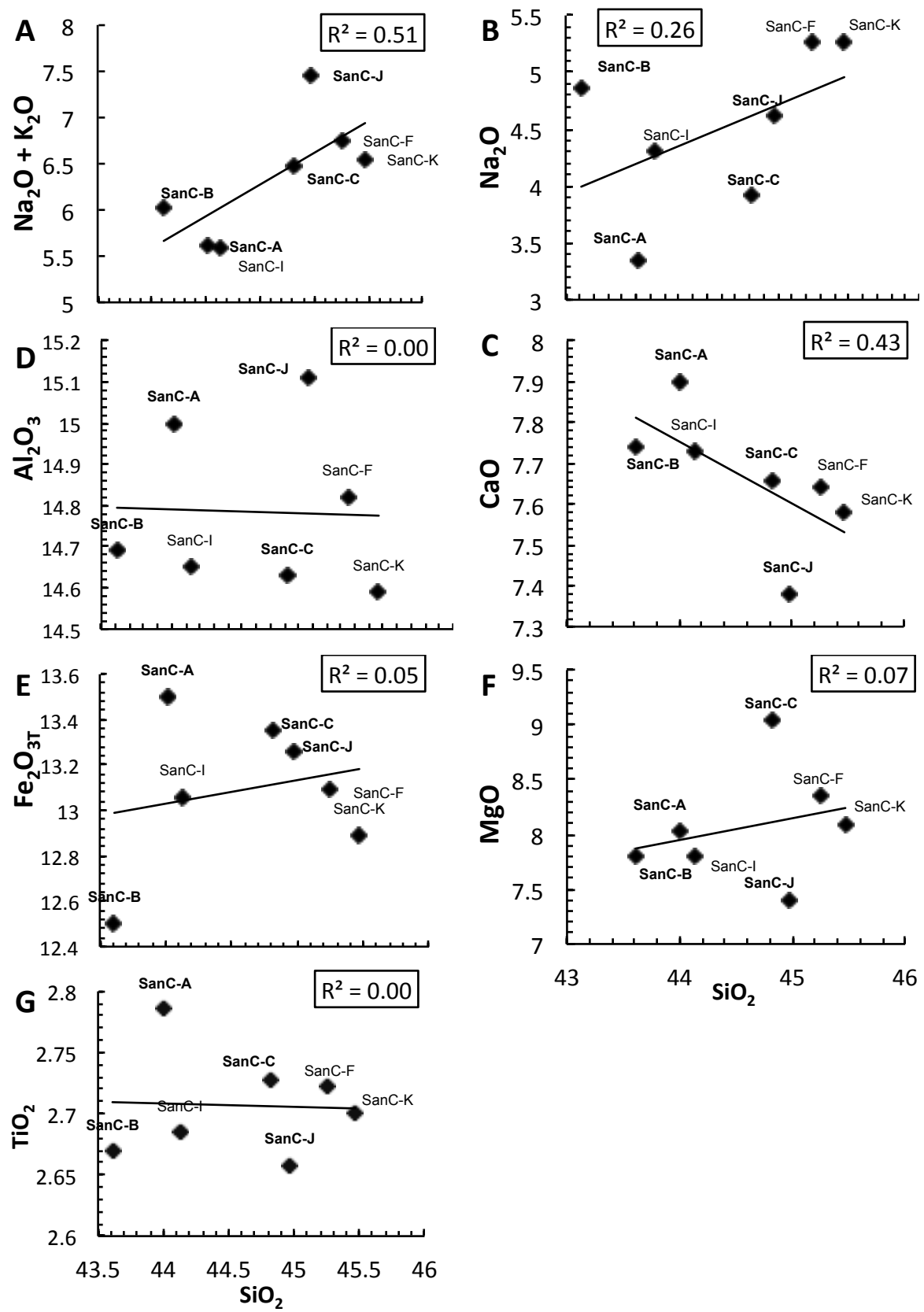
Sample C

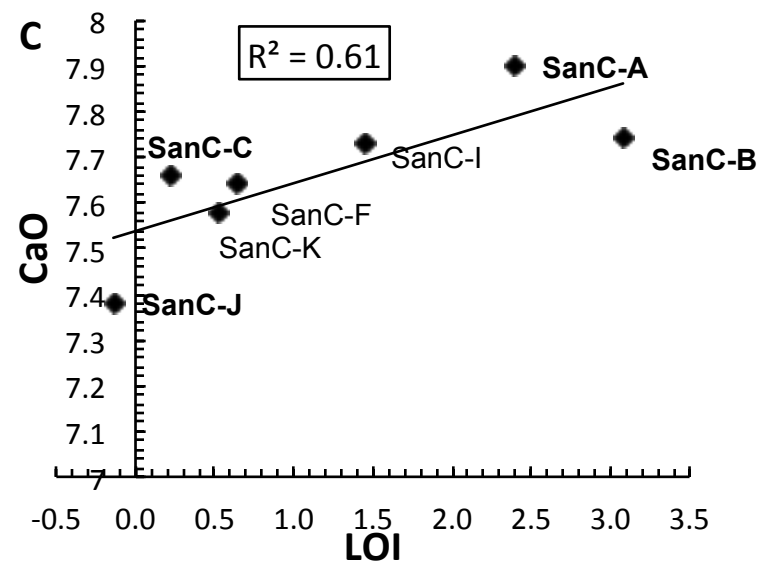
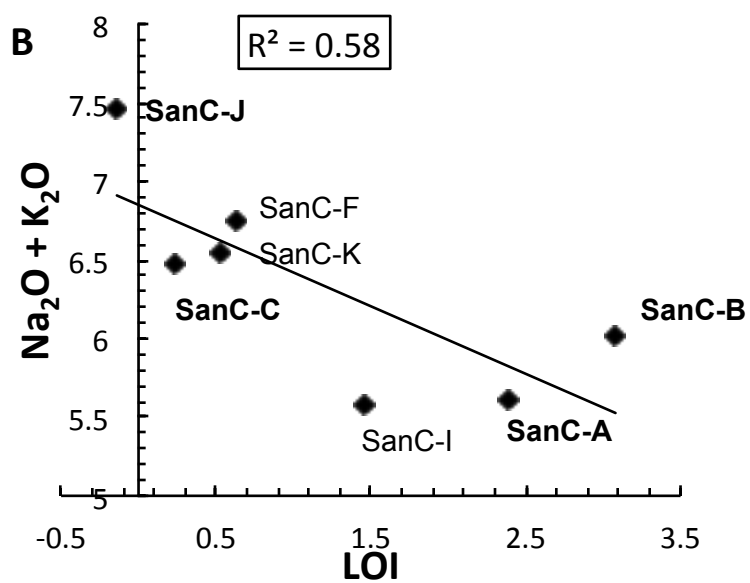
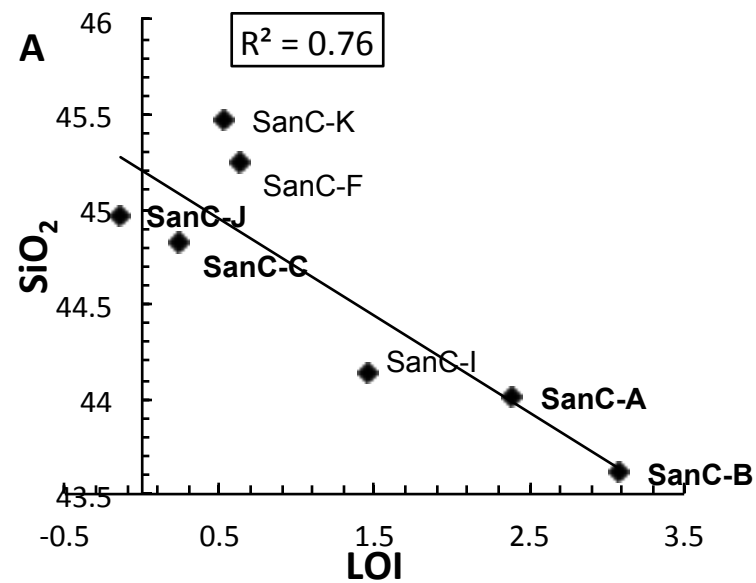
Sample B

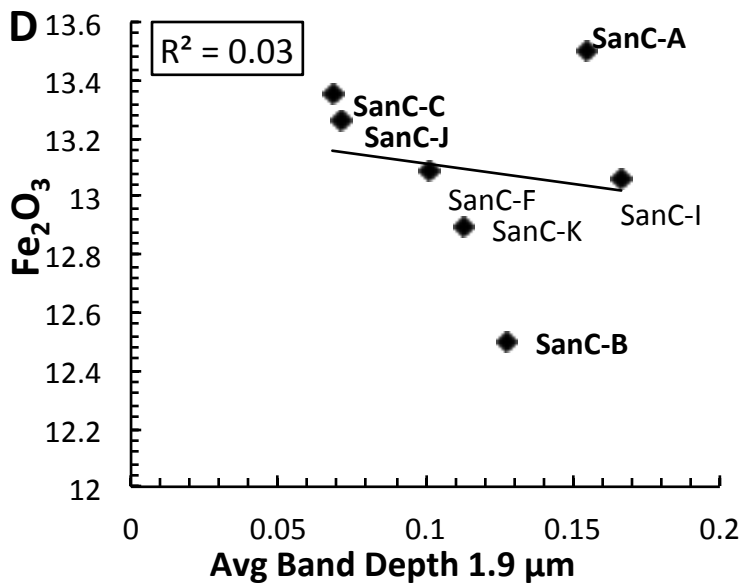
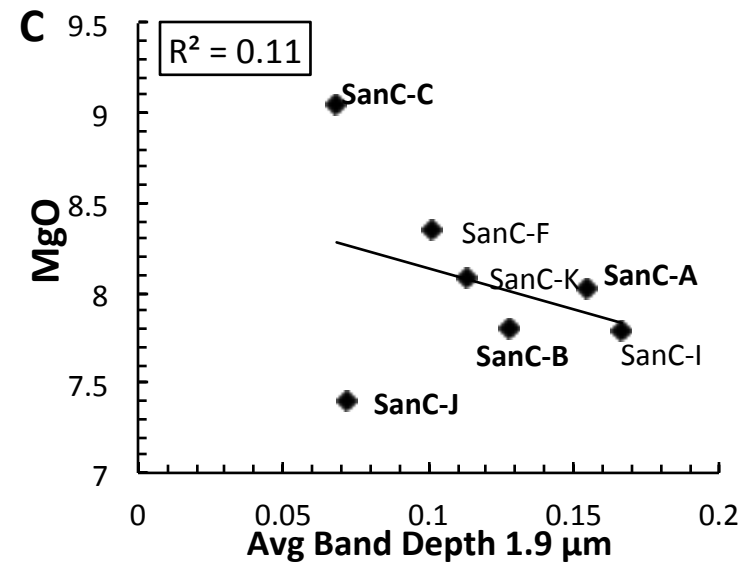
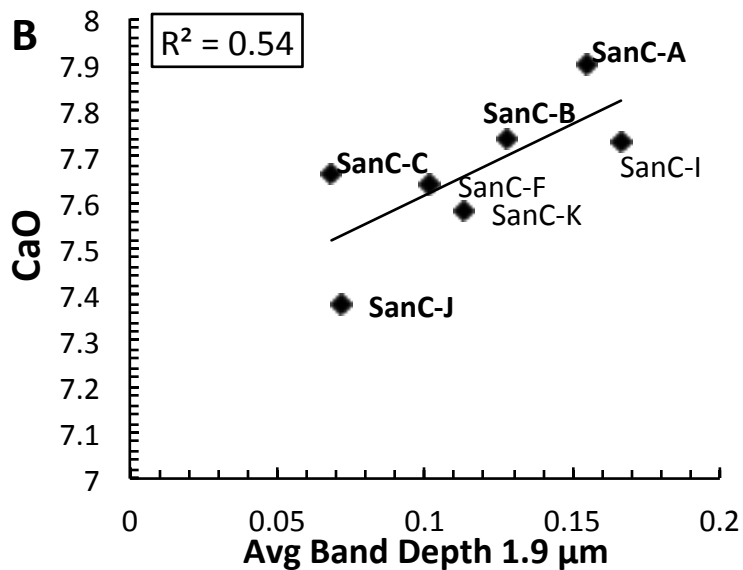
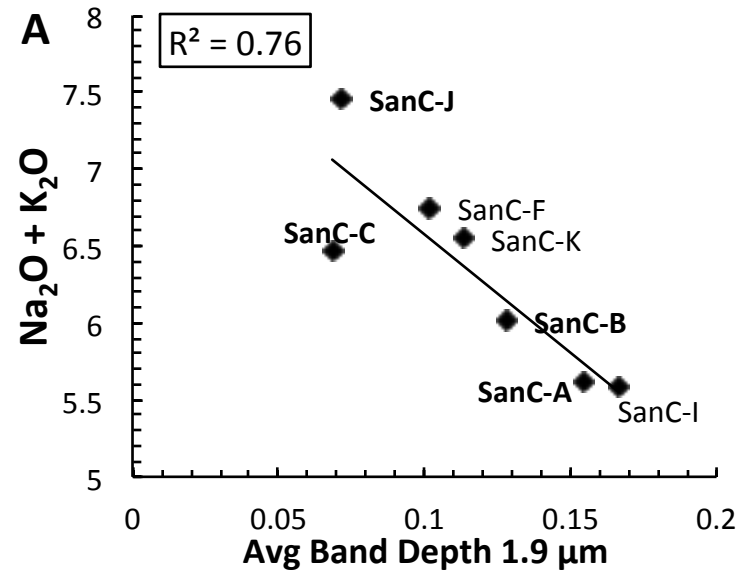
Sample A

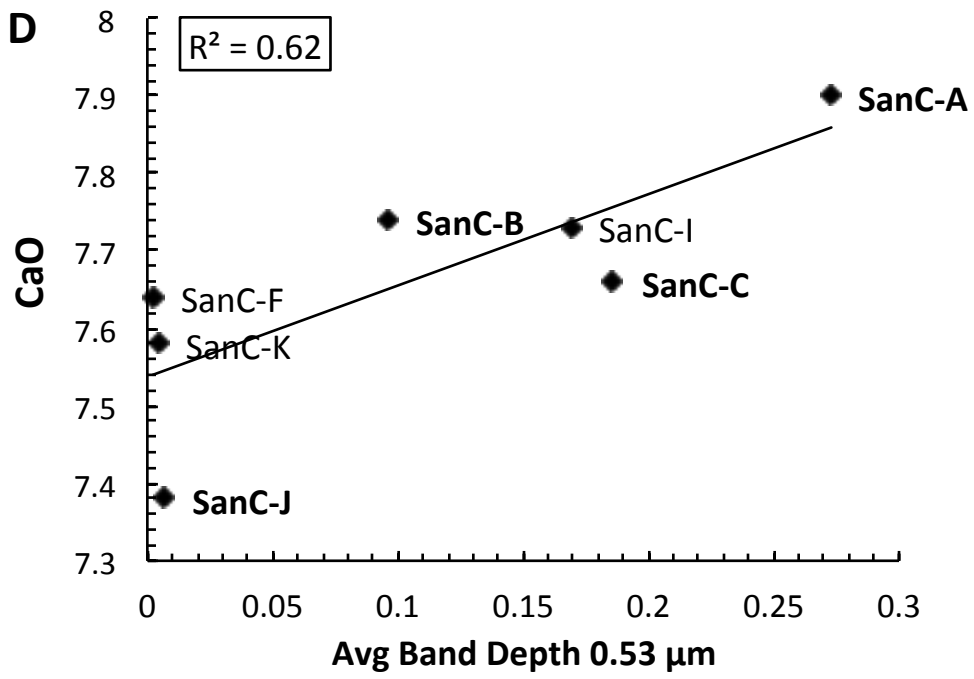
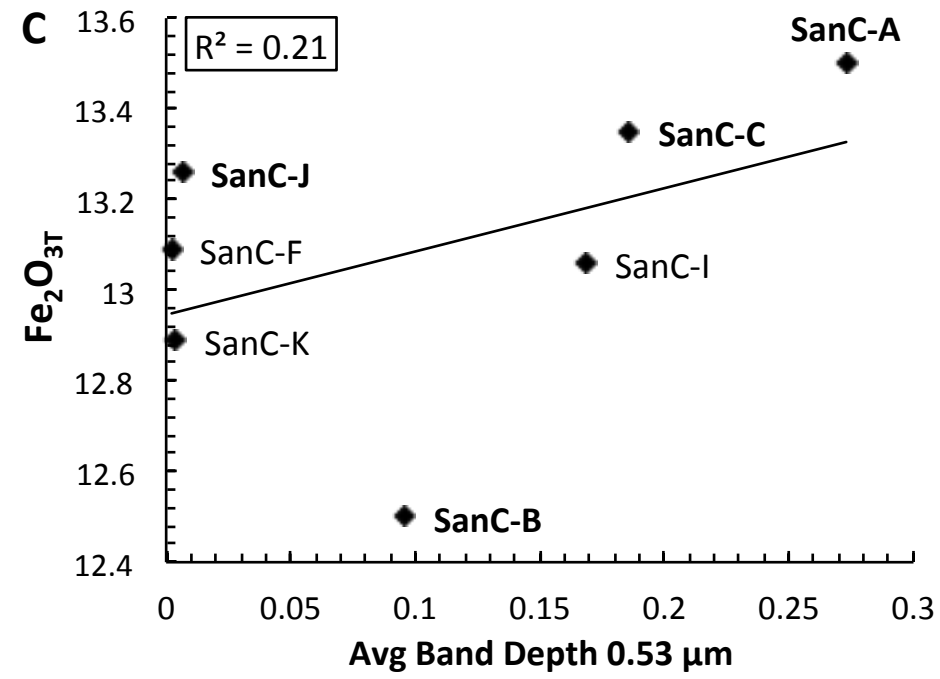
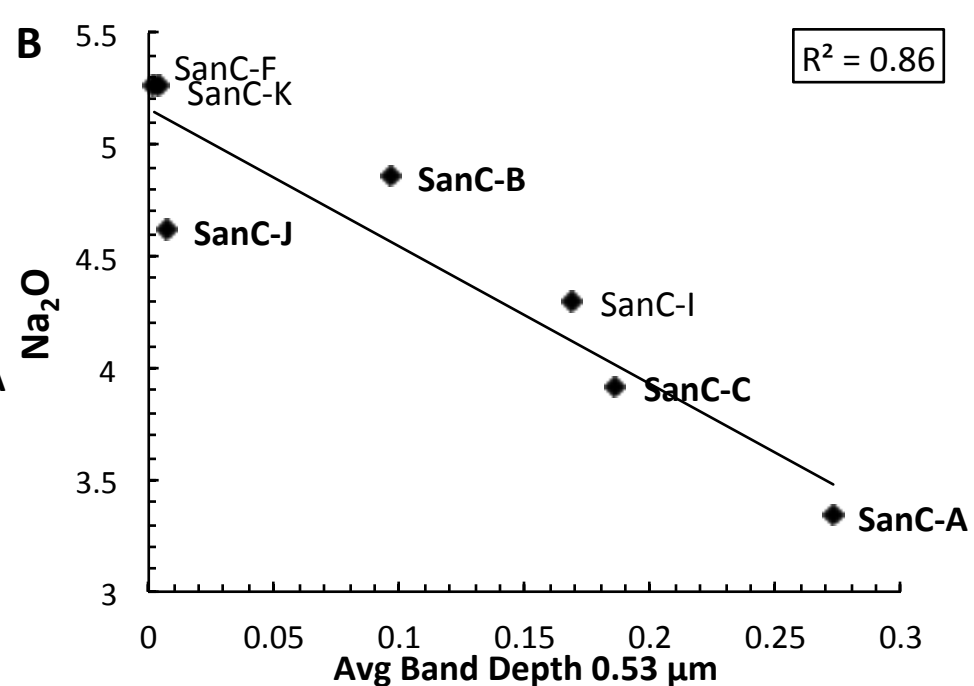
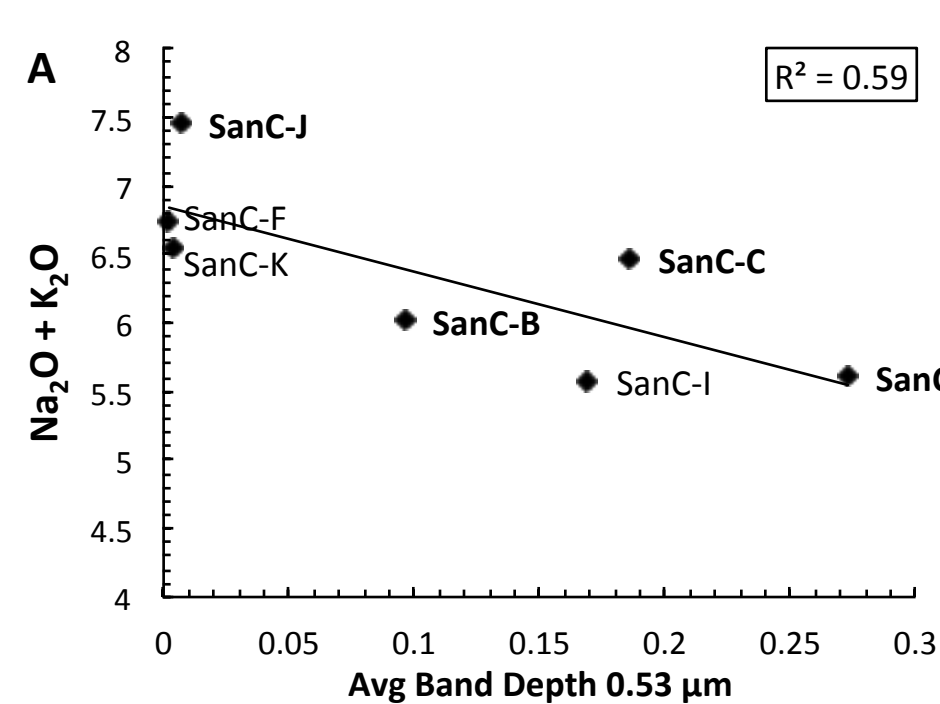


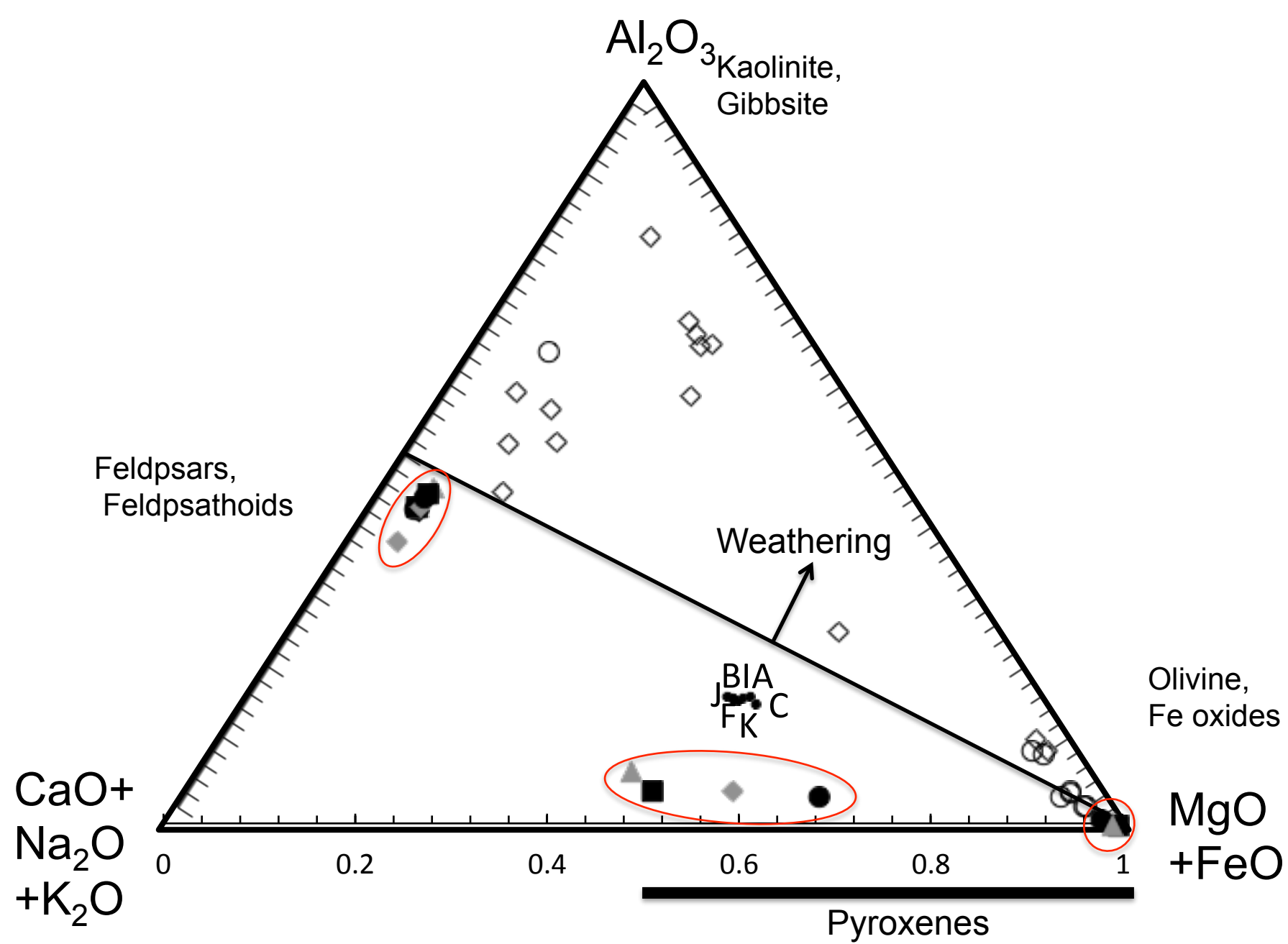
- Plagioclase
- Forsterite
- Fe/Ti Oxide
- Augite
- Nepheline
- Leucite
- Hematite
- Sanidine
- Albite
- Analcime
- Illite/Mica

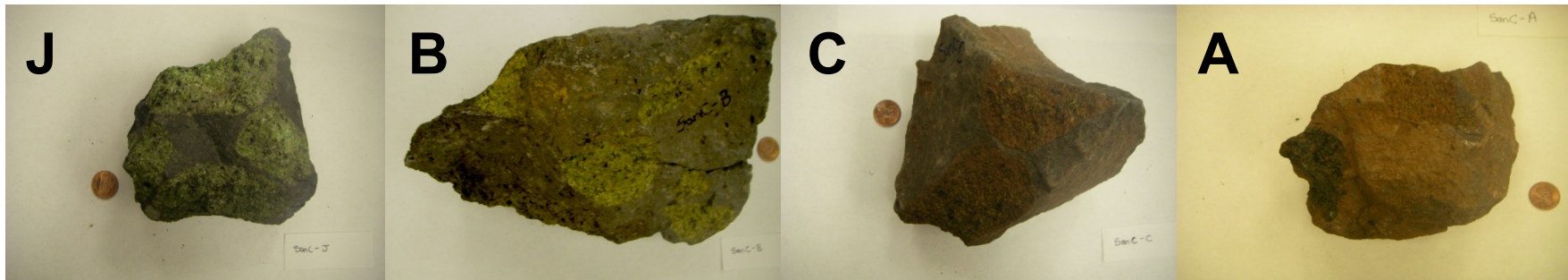










A

increasing BD1900
(hydration)

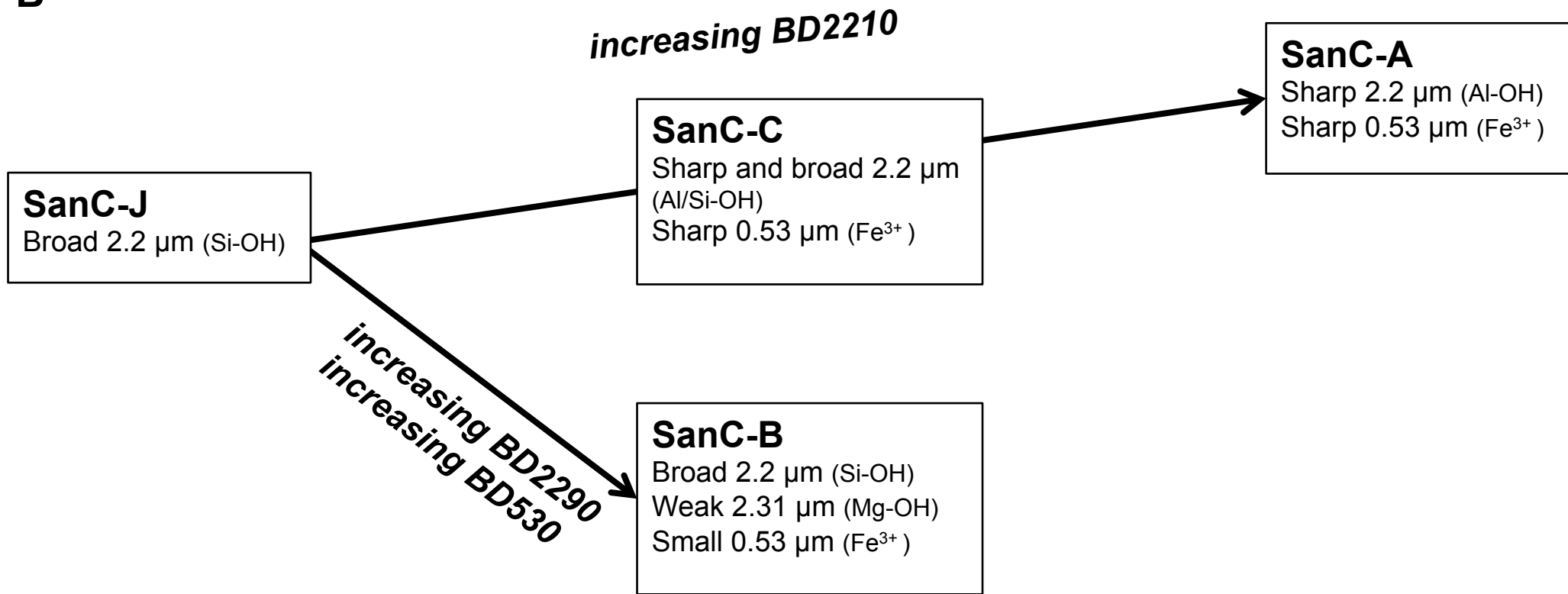


increasing BD530
(oxidation)



alkali depletion



B

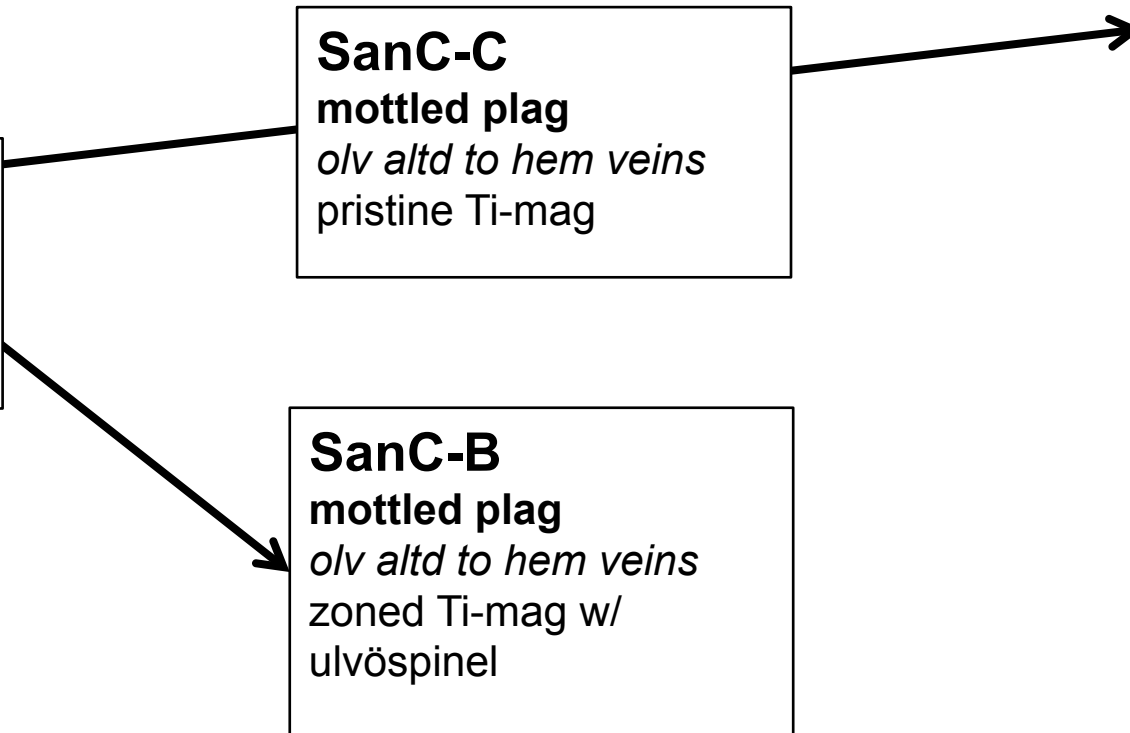
C

SanC-J
pristine plag lathes
zoned olv
pristine Ti-mag

SanC-C
mottled plag
olv altd to hem veins
pristine Ti-mag

SanC-B
mottled plag
olv altd to hem veins
zoned Ti-mag w/
ulvöspinel

SanC-A
wormy plag
olv altd to hem veins
mottled intergrowth Ti-
mag w/ ulvöspinel
Ti-mag oxidized to
Ti-hem



D

